# Sonar Detection and Classification of Underwater UXO and Environmental Parameters

**SERDP PROJECT MR-1666**
**Final Report**

Technical POC: Dr. Raymond Lim
Naval Surface Warfare Center Panama City Division, Code X11, 110 Vernon Ave.
Panama City, FL, 32407, 850-235-5178, raymond.lim@navy.mil

# REPORT DOCUMENTATION PAGE

*Form Approved*
*OMB No. 0704-0188*



| **1. REPORT DATE** *(DD-MM-YYYY)* | **2. REPORT TYPE** | **3. DATES COVERED** *(From - To)* |
|---|---|---|
| 09-07-2012 | Final report | Jan 2009 – June 2012 |

**4. TITLE AND SUBTITLE**
Sonar Detection and Classification of Underwater UXO and Environmental Parameters

SERDP Project MR-1666 Final Report

**5a. CONTRACT NUMBER**

**5b. GRANT NUMBER**

**5c. PROGRAM ELEMENT NUMBER**

**6. AUTHOR(S)**
Lim, Raymond

**5d. PROJECT NUMBER**

**5e. TASK NUMBER**

**5f. WORK UNIT NUMBER**

**7. PERFORMING ORGANIZATION NAME(S) AND ADDRESS(ES)**

Naval Surface Warfare Center Panama City Division
110 Vernon Ave
Code X11
Panama City, FL 32407

**8. PERFORMING ORGANIZATION REPORT NUMBER**

**9. SPONSORING / MONITORING AGENCY NAME(S) AND ADDRESS(ES)**

**10. SPONSOR/MONITOR'S ACRONYM(S)**
SERDP

**11. SPONSOR/MONITOR'S REPORT NUMBER(S)**

**12. DISTRIBUTION / AVAILABILITY STATEMENT**
Approved for public release; distribution is unlimited.

**13. SUPPLEMENTARY NOTES**

**14. ABSTRACT**

This report summarizes an effort carried out at the Naval Surface Warfare Center – Panama City Division (NSWC PCD) under SERDP funding to work towards resolving issues that affect sonar detection and classification/identification (C/ID) of underwater UXO using sonar. We leveraged on-going Navy sponsored sonar tests to collect data to further the model development and validation needed to keep sonar models and simulations such as PC SWAT and the more recent finite-element-based models up to date for UXO applications. This modeling capability and test data was then used both to build a database of sonar target signals useful for developing and evaluating C/ID algorithms that separate UXO from bottom clutter and to look for and understand target signatures that appear sufficiently unique for classification. While traditional C/ID based on target imaging remains an important tool, it is likely to be insufficient for small and/or buried UXO. Processing sonar target responses onto non-imaging spaces was investigated as a means to find physics-motivated clues like elastic wave signatures that don't require high resolution to provide high classification confidence. Classification analyses performed on target acoustic data collected in NSWC PCD's freshwater pond demonstrated the feasibility of class separating different targets using features derived from non-image representations of the target. Unlike image-based classification, this methodology was even shown capable of discriminating between targets of the same size and shape but different material composition.

**15. SUBJECT TERMS**
Underwater UXO, target classification, automated target recognition, target response database, physics-based feature selection, sonar simulation, sonar performance prediction, PCSWAT

| **16. SECURITY CLASSIFICATION OF:** | | | **17. LIMITATION OF ABSTRACT** | **18. NUMBER OF PAGES** | **19a. NAME OF RESPONSIBLE PERSON** |
|---|---|---|---|---|---|
| U | | | | | RAYMOND LIM |
| **a. REPORT** | **b. ABSTRACT** | **c. THIS PAGE** | UU | 45 | **19b. TELEPHONE NUMBER** *(include area code)* |
| U | U | U | | | 850-235-5178 |

**Standard Form 298 (Rev. 8-98)**
**Prescribed by ANSI Std. Z39.18**

# Table of Contents


Table of Contents ..... i
Table of Figures ..... ii
Acronyms ..... v
Sonar Detection and Classification of Underwater UXO and Environmental Parameters ..... 1
Abstract ..... 1
Objective ..... 2
Technical Approach ..... 2
Controlled pond measurements 4
Tank measurements 6
Finite Element (FE) simulation 8
Processing and ATR tools 8
Results ..... 9
Controlled measurements and data analysis 9
Tank Measurements 13
Data/model comparisons validating test tank results 20
FE development and modeling 22
Classification analysis 27
Rescoped Efforts ..... 35
Conclusions ..... 37
References ..... 39


# Table of Figures


Figure 1. The NSWC PCD freshwater pond facility: 13.7 m deep, 110 m long by 80 m wide with 1.5 m thick sand bottom. ..... 4
Figure 2. Targets used in pond scattering measurements. ..... 4
Figure 3. Basic configuration for 2009 shallow grazing angle scattering measurements. ..... 5
Figure 4. Basic configuration for 2009 high grazing angle scattering measurements. ..... 5
Figure 5. Basic configuration for 2010 shallow grazing angle scattering measurements. ..... 6
Figure 6. NSWC PCD's scaled-model acoustic tank. The photo on the right shows the empty interior along with the overhead rails, which support the sources and receivers. ..... 7
Figure 7. A c-scan track used to collect monostatic and bistatic scattering data from targets deployed on a simulated sand bottom. ..... 7
Figure 8. Scaled UXO (left and center) target and canonical target shapes (right) used in tank data collection. Targets are displayed against graph paper with 1in bolded squares. ..... 8
Figure 9. Backscatter SAS imagery processed from data collected around target broadside at a $40^o$ grazing angle. ..... 10
Figure 10. Backscatter acoustic color processed from data collected around target broadside at a $40^o$ grazing angle. ..... 11
Figure 11. Backscatter spatial frequency vs frequency plot processed from data collected around target broadside at a $40^o$ grazing angle. ..... 12
Figure 12. Comparison of acoustic color for a 2ft long x 1ft diameter solid Al cylinder processed from data collected in 2008 and 2009. ..... 12

Figure 13. Bistatic target scattering data (left) and processed imagery (right) from 2010 pond measurements. ..... 13
Figure 14. Picture (left) of 8 stainless steel 1.6 mm diameter spheres (red arrows). There is a ring, not present during the experiment, included in the photo to demonstrate the size of the spheres. Monostatic time-series data (upper right). Bistatic time-series data (lower right). The time-domain data are plotted on a dB scale. ..... 14
Figure 15. On the left is the monostatic CSAS image resulting from the upper-right time-domain data in Fig. 14. On the right is the bistatic CSAS image resulting from the lower-right time-domain data in Fig. 14. The data are plotted on a dB scale and the amplitudes have not been corrected to account for the different sensitivities of each receiver. As a result, the absolute amplitudes are not comparable between the two images but relative amplitudes against the background (i.e., SNR) may be compared..... 15
Figure 16. Picture (left) of 1/16 scale solid Al UXO replica resting on graphing paper with 1 inch large squares (the small squares are .2 inch). Monostatic CSAS image of the UXO resting proud on simulated sediment (upper right). Bistatic CSAS image of the UXO resting proud on simulated sediment (lower right). The data are plotted on a linear scale and the amplitudes have not been corrected to account for the different sensitivities of each receiver. Therefore, the absolute amplitudes are not comparable between the two images. ..... 15
Figure 17. Picture (left) of .8 inch solid Al cone resting on graphing paper with 1 inch large squares (the small squares are .2 inch). Monostatic CSAS image of the cone resting proud on simulated sediment (upper right). Bistatic CSAS image of the cone resting proud on simulated sediment (lower right). The data are plotted on a linear scale and the amplitudes have not been corrected to account for the different sensitivities of each receiver. As a result, the absolute amplitudes are not comparable between the two images. ..... 16
Figure 18. Bistatic time-series data for a free-field 1 inch diameter solid stainless steel sphere. The source and receiver configuration is shown in Fig. 7 but the angle origin is shifted by 180° from φ. The time-domain data are plotted on a dB scale normalized to the brightest pixel. Backscattering is at an angle of 180 degrees and forward scattering is at 0 degrees. The arc (green arrow) corresponding to sound that travels directly from the source to the receiver has a bright enhancement at 0 degrees when the source and receiver are perfectly aligned. Two elastic responses related to surface waves are indicated by the black and red arrows. ..... 17
Figure 19. Diagram (left) of the circular-scan setup for free-field target measurements having a monostatic source/receiver with a bistatic receiver mounted directly across the circular scan line. Both the source/receiver and the bistatic receiver are translated on a circular path simultaneously, while keeping their relative positions fixed. The bright vertical lines (black arrow) are not target related. They are the result of sound traveling directly from the source to the receiver. A stationary 5:1 .5 inch diameter solid aluminum cylinder is suspended in the center of rotation. The backscattering time-series data (upper right) and the forward scattering time-series data (lower right) are plotted as a function of aspect angle. The time-domain data are plotted with a 50 dB dynamic range and normalized to the brightest pixel in each plot. At angles of 0 and 180 degrees (red arrows) the source is broadside to the target. ..... 18
Figure 20. Time-domain free-field data for backscattering (upper left) and forward scattering (lower left). Target strength for backscattering (upper right) and forward scattering (lower right). A stationary 5:1 .5 inch diameter solid aluminum cylinder is suspended in the center

of rotation. The time-domain data are plotted with a 50 dB dynamic range and normalized to the brightest pixel in each plot. For the forward scattering target strength (lower right), the direct source-to-receiver pulse was notched out in the time domain data (lower left). The vertical null in the data caused by this notch is indicated with a black arrow..... 20
Figure 21. Time-domain bistatic scattering data (left) for a proud 2.4 mm solid stainless steel sphere plotted on a dB scale normalized to the brightest pixel. Bistatic target strength (right) from a windowed subset (black rectangle) of the time-domain data isolating the target scattering. The horizontal null (black arrows) in both plots is caused by the source blocking the receiver at 180° (backscattering), see Fig. 7 at φ = 0°..... 21
Figure 22. T-matrix simulation model predictions for the target strength (left). Measured bistatic target strength (right). ..... 22
Figure 23. Mesh refinements formulated for scattering by a proud spherical shell. ..... 23
Figure 24. Verification of COMSOL-based FE solution for scattering by a spherical shell..... 23
Figure 25. Validation of COMSOL-based FE solution for scattering by a free-field 5:1 solid Al cylinder. ..... 24
Figure 26. FE vs measurement comparison for scattering by a 5:1 solid Al cylinder deployed proud on the sand bottom of the NSWC PCD freshwater pond. ..... 25
Figure 27. Comparison of FE simulated and measured free-field target strength plots for WSU's "paddle." ..... 25
Figure 28. The orientation of the paddle for data generated and collected for Fig. 27. The source field is incident into the page and $0^o$ aspect = broadside. ..... 26
Figure 29. 3D FE simulation of scattering by artillery shell embedded in a sand bottom with a $25^o$ tilt. Plots of total field (left) and backscatter target strength vs. frequency and aspect angle (right) are shown for a plane wave incident at a $23.27^o$ grazing angle. ..... 26
Figure 30. PC SWAT is used to imbed targets on the featureless bottom (above left) into the imported image from a previous field survey (above right). ..... 27
Figure 31. Isolation of selected target signals from noisy data..... 28
Figure 32. Subtracting the isolated target signal from the original signal. ..... 29
Figure 33. Among a set of 3 like- shaped cylinders, a feature selection tool is applied to look for phenomena in the acoustic color of each target (top row) that is unique to that target (white or black regions in the corresponding plot below). ..... 30
Figure 34. Excitation of surface Rayleigh waves at $-27^o$ target aspect on a solid Al cylinder produces quasi-periodic structure in its target strength plot. ..... 30
Figure 35. Process for using elastic information in sonar data to discriminate between 4 cylindrical targets with the same size and shape. ..... 31
Figure 36. Silhouette plot of four clusters in 5 dimensional feature space. ..... 32
Figure 37. An example of time-frequency processing of data (upper left) collected in NSWC PCD's pond facility for the Al artillery shell. The time-frequency transform of a windowed segment of the red ping is shown in the upper right. A thresholded template is shown in the lower left. A composite of 8 templates are overlaid in lower right. ..... 34
Figure 38. Bar graph demonstrating class separation of data from 5 targets based on templates of high intensity regions in time-frequency space. Percent match is computed as the ratio of the target template area overlapping segment highlights of the test ping to the total target template area. The % match averaged over all 8 pings in the random set is shown above.. 35
Figure 39. Schematic of the NSWC PCD Acoustic Pier Facility including the sediment tank (blue) to be deployed at the bottom of the lined freshwater pool. Sonar hardware suspended

from the rotator moved along the overhead rail (red) would be able to detect targets in the tank at high grazing angles. ..... 36
Figure 40. Pictorial of the sediment tank designed for high-grazing-angle data collection from bottom targets. ..... 37

## Acronyms

Al - Aluminum
APL-UW – Applied Physics Laboratory at University of Washington
ATR – Automated Target Recognition
BU – Boston University
CAC – Computer Aided Classification
CAD – Computer Aided Detection
C/ID – Classification/Identification
CSAS – Circular Synthetic Aperture Sonar
c-scan – circular line-scan
COMSOL – software trade name, formerly FEMLAB
FE – Finite Element
FEM – Finite Element Method
FY – Fiscal Year
IEEE – Institute of Electrical and Electronics Engineers
kHz – kiloHertz
MATLAB – MATrix LABoratory numerical computing software marketed by Mathworks
NCSC – Naval Coastal Systems Center
NSWC PCD – Naval Surface Warfare Center Panama City Division (formerly CSS and NCSC)
ONR – Office of Naval Research
PC SWAT – Personal Computer Shallow Water Acoustic Toolset
ROI – Region Of Interest
SAS – Synthetic Aperture Sonar
SNR – Signal-to-Noise Ratio
SON – Statement of Need
T-matrix – Transition matrix
UXO – UneXploded Ordnance
WSU – Washington State University
X – NSWC PCD organizational code

# Sonar Detection and Classification of Underwater UXO and Environmental Parameters


## Abstract

*Objective*: The objective of the current research is to work towards resolving issues that affect sonar detection and classification/identification (C/ID) of underwater UXO using sonar.
*Background*: Based on extensive assessments of other sensor technologies carried out at NSWC PCD for underwater Navy applications, sonar is expected to play an indispensible role in underwater UXO remediation. Acoustics can be used to probe for targets over a significant range and, being a wave phenomenon, can be used to image buried targets for discrimination from clutter. However, environmental factors can make detection and discrimination problematic, often making imagery insufficient to discriminate targets from clutter.
*Technical Approach:* We leverage on-going Navy sponsored sonar tests to collect data to further the model development and validation needed to keep sonar models and simulations such as PC SWAT and the more recent finite-element-based models up to date for UXO applications. This modeling capability and test data is then used both to build a database of sonar target signals useful for developing and evaluating C/ID algorithms that separate UXO from bottom clutter and to look for and understand target signatures that appear sufficiently unique for classification.
*Results:* Work carried out during 2009-2011 covered four primary areas: controlled pond and tank measurements, finite element (FE) development and modeling, classification analysis, and a laboratory study of muddy sediments. Sonar target data in both monostatic and bistatic configurations were collected at NSWC PCD's freshwater test pond in 2009-2010, which were processed to provide representations of target intensity in a variety of spaces (coordinate space for imagery, frequency vs target aspect, frequency, vs time, etc.). Data were also collected within NSWC PCD's small-scale test tank on a 1/16-scale UXO and other simple target shapes in 2011 to study more diverse scattering configurations not accessible in the full-scale measurements. FE algorithms were developed and used to generate plots of target strength as a function of aspect angle and frequency to compare with the experimental results. FE represents another cost effective alternative to field measurements for creating databases of real target and clutter responses needed for classification analysis. Classification analyses performed on target acoustic data collected in the freshwater pond demonstrated the feasibility of class separating different targets using features derived from non-image representations of the target. Unlike image-based classification, this methodology was even shown capable of discriminating between targets of the same size and shape but different material composition. Finally, research carried out by Boston University to estimate or measure the environmental parameters of muddy sediments needed in sonar simulations has resulted in an electro-chemical model of mud that explains sound speed and attenuation trends seen in data.
*Benefits:* A substantial database of target responses is often required to train and test C/ID algorithms. The data collected here augment existing databases and the models developed and validated enable further augmentation through simulation. Furthermore, this work supports a physics-based understanding of target responses to enable better selection of classification features, which would be more robust against environmental factors. These efforts respond to SERDP SON MMSON-09-01.

## Objective

MMSON-09-01 specified needs for studies focusing on "wide area assessment" and the "acoustic response of munitions and environment" in underwater areas. The research performed in this project responds to these points by investigating issues associated with using sonar as a tool for finding and characterizing UXO. Sonar has been the Navy's workhorse for detection and discrimination of underwater objects from clutter through analysis of image features. However, new features need to be identified for UXO due to their more varied shapes and sizes, and difficulties arise for buried ordnance (like most UXO) because the wave attenuation and inhomogeniety in ocean sediments make detection less predictable and high-resolution imaging more difficult. Even when imaging can be done, important image features (e.g., highlight/shadow features) are lost. Therefore, modeling, data collection, and data analysis is performed as a primary component of this project to develop the understanding of factors that affect the acoustic response of proud and buried munitions when searched with both side-scan sonar used for wide area assessment and bottom-looking sonar for detection of completely buried targets. The knowledge gained would be used to

- test new ways to improve signal-to-noise (SNR) against targets
- improve ability to discriminate UXO from clutter
- validate simulation software for generating sonar data
- enable UXO sonar performance prediction.

A particular interest in this effort is on identifying target phenomena yielding features with robust discriminatory power for separating UXO from clutter. This final report will summarize the results obtained towards these goals based on the modeling, data collection, and data analysis performed during this project.

## Technical Approach

The approach taken to enable wide area assessment of UXO contamination with sonar is to build a high fidelity simulation capability that can be used to test overall performance of various sonar under varying conditions. At NSWC PCD, simulation of image-based sonar performance has generally been carried out using software such as the Personal Computer Shallow Water Acoustic Toolset (PC SWAT), so improving and validating this software for UXO applications with insight gained from modeling and data analysis continues to be done as needed. However, growing concerns over small or buried targets that are difficult to image to the resolution needed for effective classification has driven a need to extract either more or different information from the target response. To meet this need, this project investigates and compares the detection and discriminatory potential of target information collected and/or processed and combined in different ways.

The best information to extract from the target response and the best sonar configuration to obtain it remains to be determined. However, recent efforts fusing target aspect and spectral characteristics from backscatter echoes has been shown to yield potentially good features for distinguishing targets from clutter. This was demonstrated by training statistical pattern recognition algorithms such as support vector machines and relevance vector machines with

feature vectors extracted from representations of the target strength in aspect vs frequency space. Thus, high resolution imagery is not required. While use of these statistical tools for automated target recognition (ATR) is growing, a danger is that insufficient training can produce good classification using existing data sets with little assurance of robustness against new data sets. Robust discrimination depends on training with data sets that sufficiently sample the range of feature variability exhibited by targets and clutter, which is typically not known *a priori* and can require a large amount of training data. Because collecting sufficient data for training can be very costly, the approach taken to help test the ATR component of sonar performance combines results of several efforts to make sure a diverse set of data for classifier training and testing is created. First, dedicated UXO and clutter acoustic measurements in NSWC PCD's pond facilities (Fig. 1) are carried out in both monostatic and bistatic configurations to provide a controlled but diverse dataset of realistic target responses. This is further supplemented with leveraging the Navy's investment in the development of an efficient, high-fidelity, Finite Element (FE) simulation capability to accommodate complex targets in realistic environments. Physics-based interpretations of target responses are used to select target characteristics for ATR use. The premise is that training data requirements can be reduced if target characteristics known to be unique to UXO can be found. Measurements in a small-scale test tank utilizing small targets on a fine-grained bed of sediment were also utilized to compare target physics in different scattering configurations. Scattering configurations yielding strong signals that target physics provides a clear connection to target elastic properties are desired.

In addition to these efforts, Boston University (BU) completed a study of mud sediments initiated to enable remote estimation of acoustic parameters needed in sonar simulations in muddy environments. In their research, an electrochemical model of mud is combined with an effective medium model to include compressibility effects due to entrained bubbles. The presence of bubbles is known to be an important factor in decreasing the sound speed, which is an important input parameter that is not easily estimated for muds. Past measurements of the sound speed characteristic of the high porosity Dodge Pond mud were found to have a sonic speed less than that observed by Wood and Weston (1); i.e., a compressional speed 3% less than that of water. Other experiments performed on muddy sediments at frequencies greater than a kilohertz are consistent with the Dodge Pond observations when micro-bubbles are present. Observed speeds of gas bearing mud were typically $C_{mud} \sim (0.91\text{-}0.97)C_w$. A theoretical treatment of "muddy sediments," the Card House Theory (2), is proposed to estimate the slow sound speed and frequency dispersion as a function of mud porosity. The presence of micro-bubbles can lower the sound speed consistent with the Mallock-Wood equation when the bubble size distribution and mean bubble separation are less than the wavelength of the propagating wave. Since measurement of the bubble size distribution within mud is difficult, theoretical limits on the size distribution in the complex card house structure can be useful in interpreting measurements on muddy sediments.

Except for BU's work, more details on the approach taken for these efforts follow. A complete description of BU's objectives, approach, and results are provided in their final report (3), which is attached in the Appendix.

**Figure 1. The NSWC PCD freshwater pond facility: 13.7 m deep, 110 m long by 80 m wide with 1.5 m thick sand bottom.**

**Controlled pond measurements:** Drs. J. Kennedy and J. Lopes performed pond measurements in NSWC PCD's pond facility (Fig. 1) in collaboration with researchers from the University of Washington Applied Physics Laboratory (APL-UW) (Drs. S. Kargl and K. Williams) and researchers from Washington State University (WSU) (Prof. P. Marston). Bottom target scattering measurements were carried out on a set of realistic and canonical shaped targets (Fig. 2) chosen to allow both variety for ATR analysis and simplicity for benchmarking and facilitating physical interpretation. Measurement configurations were set up to collect data in monostatic (co-located source and receiver) and bistatic (not co-located) modes against targets

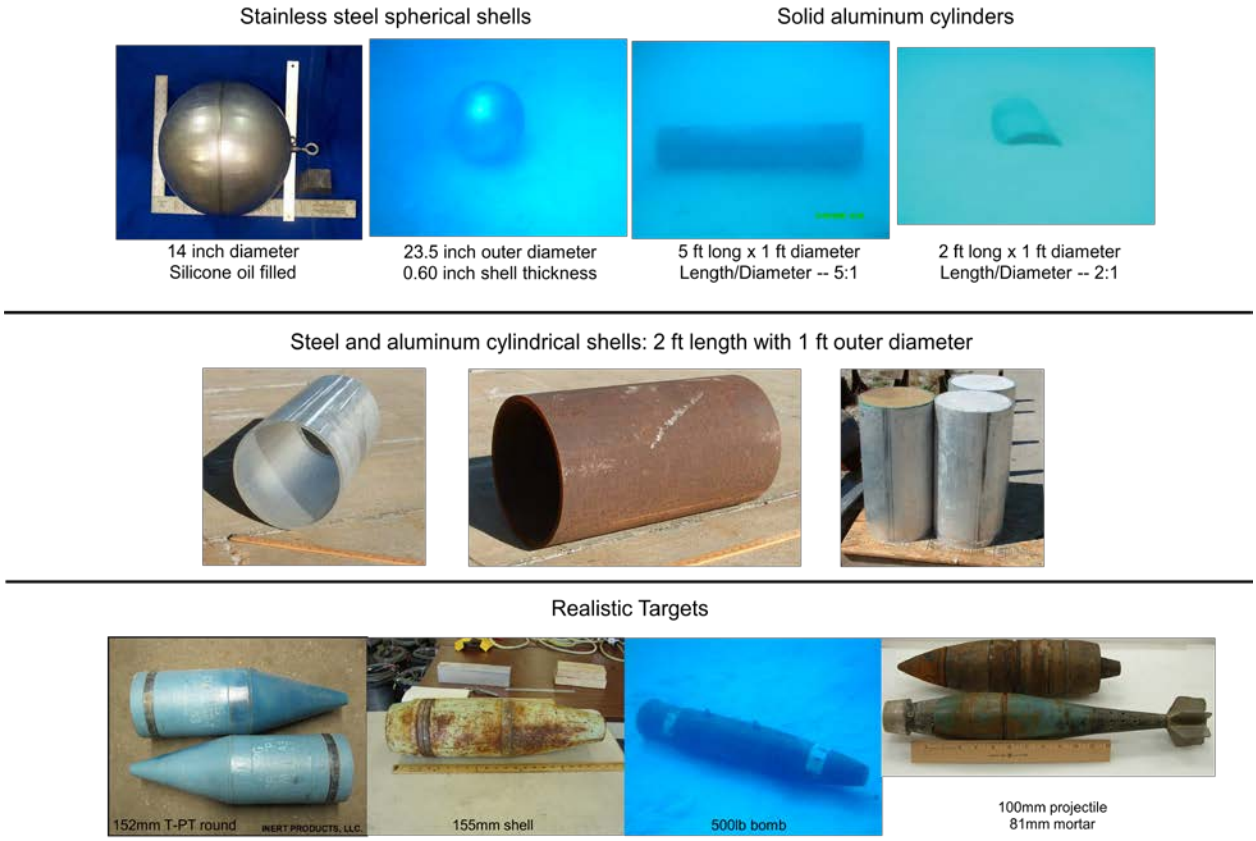


**Figure 2. Targets used in pond scattering measurements.**

that were both proud and buried and illuminated at above and below the critical grazing angle of the bottom. Targets were typically oriented with their axes parallel to the bottom surface but some data on a cylinder tilted up at the surface was also collected. In 2009, shallow-grazing angle data were collected by the NSWC PCD/APL-UW/WSU team using two rails deployed on the sand bottom in a basic arrangement as depicted in Fig. 3. Sources and receivers attached to towers moved along the rails allowed synthetic aperture sonar (SAS) data to be collected over a frequency band of 3-50kHz. The rail lengths allowed both monostatic and bistatic data to be collected over a 90$^{o}$ aspect range, although full 360$^{o}$ looks at each target were achieved by having divers rotate the target.

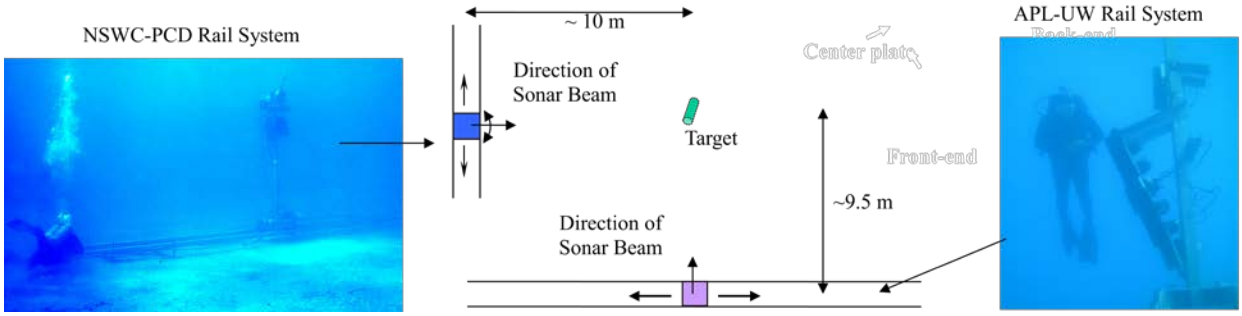


**Figure 3. Basic configuration for 2009 shallow grazing angle scattering measurements.**

In 2009, a set of high-grazing angle data were also collected by NSWC PCD on the set of 2ft-long cylinders shown in Fig. 2 using the single-rail backscatter configuration depicted in Fig. 4. The targets were deployed both proud and buried and oriented parallel to the rail. The ground ranges shown allowed data collection at nominal bottom grazing angles of 30$^{o}$ and 40$^{o}$ when the sensor platform was closest to the targets.

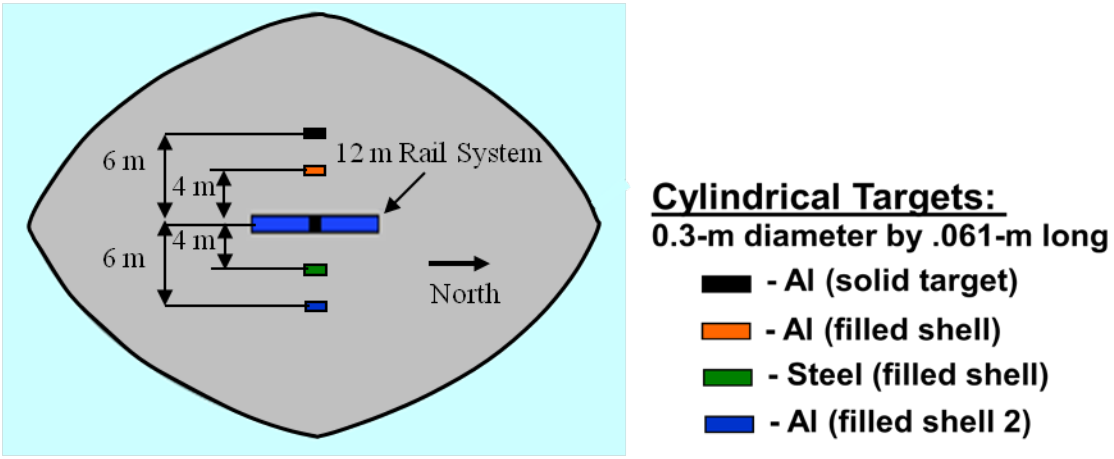


**Figure 4. Basic configuration for 2009 high grazing angle scattering measurements.**

In 2010, another data collection effort by the NSWC PCD/APL-UW/WSU team was set up in NSWC PCD's pond using a different layout to collect shallow angle data more efficiently. Multiple targets were deployed at 1.5m or 3m intervals parallel to APL-UW's rail and filtering algorithms were used in post processing to separate the various target signals. This is depicted in Fig. 5 along with the set of targets used. Monostatic and bistatic signals from the full range of aspect angles on each target were collected, employing divers to rotate the targets at 20$^{o}$ intervals.

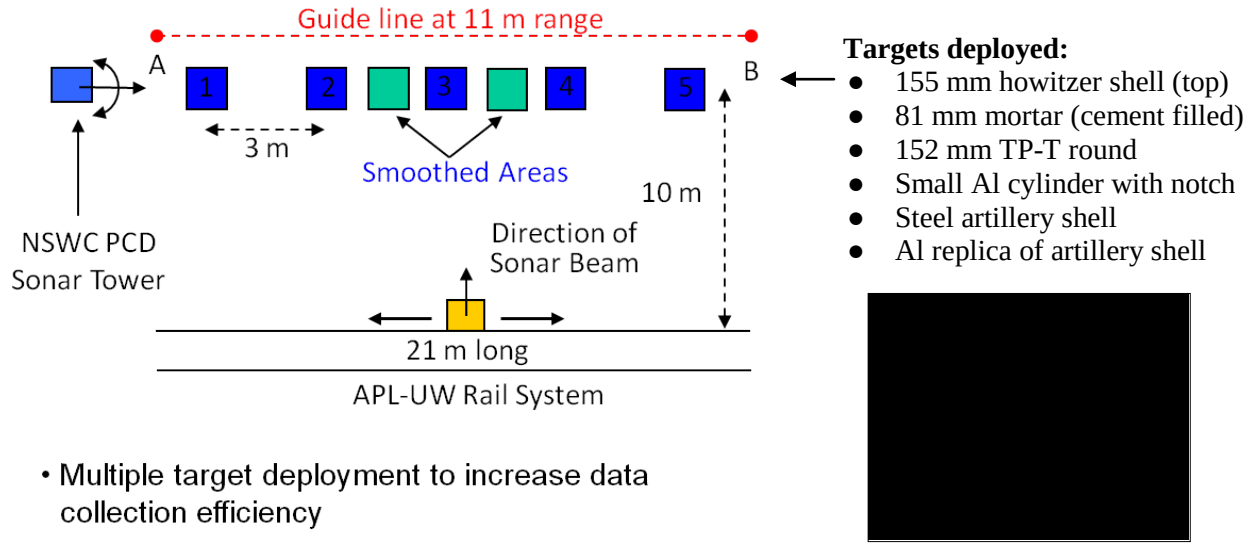


**Figure 5. Basic configuration for 2010 shallow grazing angle scattering measurements.**

Finally, in 2011, an ONR-funded target scattering measurement in NSWC PCD's test pond was leveraged to support SERDP UXO data collection for targets in a half buried configuration. This data complements the proud and buried measurements on similar targets carried out in the past. Two targets at a time were deployed and rotated from -80 to +80 degrees in 20 degree steps while monostatic SAS data was collected using sources and receivers mounted on NSWC PCD's rail. Four UXO targets total were deployed over the 6 days of testing: the Al artillery shell replica, the steel artillery shell replica, the 155 mm howitzer shell, and the slotted Al cylinder.

**Tank measurements:** In 2011, leveraging an ONR-funded research effort, a circular line-scan (c-scan) capability was designed, constructed and automated in NSWC PCD's small-scale test tank (Fig. 6) to explore the utility of multistatic geometries involving circular scans. The tank measures 8ft wide x 12ft long x 8ft deep and is fitted with overhead rails supporting a computer-controlled mount that can be moved down the rails or rotated in a horizontal plane. Sources and receivers can be suspended from rods at the end of a cross beam attached to the mount to implement a circular scan track. One c-scan geometry is shown in Fig. 7. The bistatic receiver is held in a fixed location, while the monostatic source/receiver is scanned along a circular track. This configuration permits simultaneous measurement of monostatic and bistatic target scattering. Targets are placed in the center of rotation and the data are processed to produce circular synthetic aperture sonar images and target strength vs. aspect angle. A 1.5in layer of fine glass beads held in a 2ft- square wood tray is used to simulate a sand bottom when needed.

Measured sound speed, density, and attenuation within the simulated sand (see Fig. 7) were confirmed to be within realistic bounds when the frequency band used in the tank (~50kHz-1.5MHz) is scaled down to the desired frequency band for full sized targets.

A set of scaled targets consisting of aluminum cylinders, steel spheres, an aluminum cone, and 3 machined 1/16$^{th}$-scale UXO shapes were used in the tank measurements. The UXO shapes were copies of the 100 mm steel artillery shell seen in Fig. 5, machined out of aluminum, brass, and steel. These targets are shown in Fig. 8.


**Figure 6. NSWC PCD's scaled-model acoustic tank. The photo on the right shows the empty interior along with the overhead rails, which support the sources and receivers.**

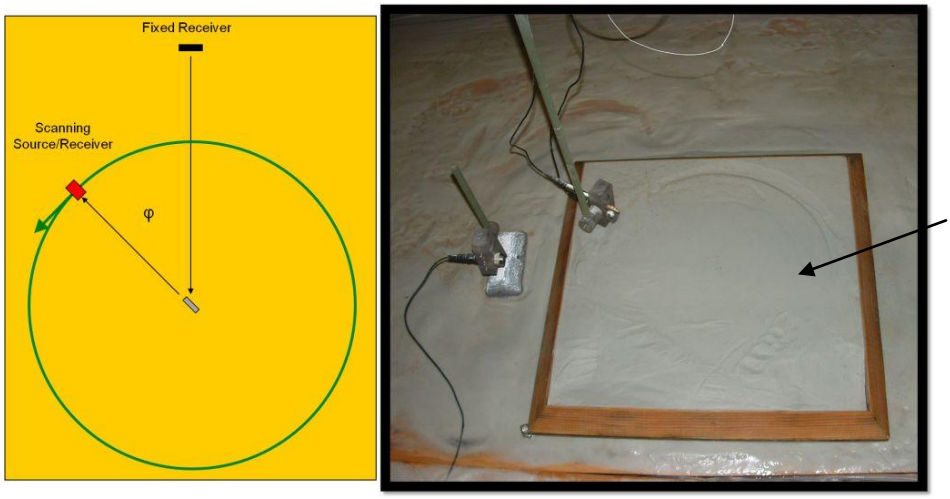


**Figure 7. A c-scan track used to collect monostatic and bistatic scattering data from targets deployed on a simulated sand bottom.**

**Figure 8. Scaled UXO (left and center) target and canonical target shapes (right) used in tank data collection. Targets are displayed against graph paper with 1in bolded squares.**

**Finite Element (FE) simulation:** Development of a capability to carry out finite element simulations for realistic targets on or in the seafloor has been funded for several years at NSWC PCD by the Office of Naval Research (ONR). Both our last SERDP project (MR-1506) and the present project has leveraged this work to help extend its use for building a database of UXO target signatures. The approach taken so far has been to develop and check a set of algorithms written for the COMSOL Multiphysics software package. These produce highly efficiently gridded solutions for elastic targets on or buried under a typical ocean bottom. Solution grid configurations and sizes were formulated to maintain uniform error across specified frequency bands. Reduced grid size formulations taking advantage of target symmetries were introduced. Boundary conditions that allowed reduced FE volume sizes around elongated targets were derived and tested. Coupling the FE solutions to analytic propagation formulas based on the Helmholtz equation was performed to allow fast simulations out to long ranges. Verification and validation of much of these FE components on a set of proud and buried canonical targets (spheres and cylinders) was performed by comparing against benchmarks computed with transition matrix solutions. Tests of the existing FE system have mostly been run on dedicated workstations but the current FE software has recently been transported to a scalable architecture, 25 processor, multi-blade rack computer. Thus, computational turnover has been increased by a factor of 25 by distributing portions of long runs among the processors. With incorporation of the latest COMSOL upgrade, parallel processing of complex problems should also be possible, although implementation of this capability remains to be tested.

**Processing and ATR tools:** While the measurements and FE simulations performed will provide data that can be used to train and test ATR algorithms for non-image based classification, software tools were also developed to increase the effectiveness of this data. A capability has been developed into PC SWAT to imbed target data either collected or simulated into imagery from past field surveys; thus, making available an infinite number of new target-in-environment combinations that can be processed for imagery or other target spaces to be fed into ATR classifiers. This is further enabled by developing and applying algorithms for isolating target signals from given measured data sets so they can be swapped or recombined into new data sets. This processing ignores multiple scattering effects between targets but this is usually a good approximation where targets are not very close. The resulting target signal isolation algorithms also make data collection more efficient by allowing simultaneous sonar measurements on multiple targets within a limited area. Even though their signals overlap in the raw SAS data, signals for each target can be separated and subsequently processed into imagery or aspect vs frequency space for feature extraction. A Matlab toolbox was written based on these signal

isolation algorithms to enable manipulation of the target and clutter data collected at the NSWC PCD pond. The newly created data can be stored as a database containing reverse beamformed "raw" data, SAS beamformed imagery, and frequency-aspect responses.

In addition to sharing the pond data collected with both APL-UW and other ONR funded researchers at NSWC PCD for ATR analysis, a SERDP funded ATR component was carried out at NSWC PCD, focused on taking advantage of physics-motivated features to class separate UXO targets. The ATR approach here emphasized non-imaging techniques to complement existing image-based methods. It also emphasized feature selection rather than classifier development because the technology for classifiers is considered mature enough that significant improvements in ATR reliability (i.e., more robust class separation) are expected to come from better selection of features used in training. Implicit in this is that the choice of classifier to train is not as important as the features selected to train with. Therefore, the classifier used to test class separation performance in the results discussed below is not chosen based on the state-of-the-art but, rather, on the one most intuitive to implement for the feature set chosen.

New features from the collected pond data that are characteristic of a target's elastic properties or that arise from viewing the target in a new way were sought and assessed. Features are generally deduced from phenomena seen in a space of some measured target property as a function of one or two other parameters varied in the data collection; e.g., target strength as a function of target aspect and frequency. To facilitate selection of feature vectors for classification analysis, various methods were used to augment elastic signals and view target phenomena among different targets to assess how well those phenomena differentiated the targets.

Two types of features were tried in the work reported here. First, features extracted from plots of target strength vs. target aspect and frequency that are associated with elastic surface waves excited on cylindrical targets were fed into a K-means clustering algorithm to demonstrate their effectiveness in distinguishing 4 like-shaped targets of differing material construction. In a second study, simple target energy threshold masks that have been filtered to remove target specular reflections and statistically "orthogonalized" through training in time-frequency space were shown to be effective at distinguishing between backscatter signals from several UXO projected onto time-frequency space.

## Results

Results from project MR-1666 are described below according to the major tasks performed: controlled measurements and data analysis, FE development and modeling, and classification analysis.

**Controlled measurements and data analysis:** Two major test events were carried out during 2009 and 2010 in collaboration with APL/UW and WSU in NSWC PCD's freshwater test pond. These involved targets deployed on a flat sand bottom at various depths. SAS data were acquired using both monostatic and bistatic scattering configurations to investigate the potential advantages of nonstandard sonar detection and classification configurations. Some initial results and analysis of data from the pond tests were published in papers (4) and (5), which are attached in the Appendix for further detail. To assess the relative advantages of different representations

of the target, the data were processed in three ways: imagery, projections onto target aspect angle vs frequency ("acoustic color") space, and projections onto spatial frequency vs frequency space. The last is produced as an intermediate step in wavenumber algorithm beamforming (6) and is, therefore, of interest for extracting additional target information that efficiently complements imagery. Examples of these representations are shown in Figs. 9-11 for backscatter by 4 proud targets (2ft Al cylinder, 2ft pipe, bullet shape, and mortar) insonified at $20^o$ and $40^o$ grazing angles.

In general, all three representations of the 4 targets produce useful distinguishing characteristics. For example, in Fig. 9, the cylindrical shapes are easily distinguished from the bullet and mortar by their shape and dimensions, even when observed at different grazing angles. Even the two cylinders exhibit distinctly different reverberation and elastic reradiation patterns. However, despite adequate SNR for detection, the smaller bullet and mortar shapes are more difficult to distinguish between because the resolution is insufficient to produce unambiguous shapes and dimensions. For these targets, representations like those in Figs. 10 and 11 may be more useful because they focus on properties of the isolated target signal rather than using image characteristics that depend on differences between signals from various parts of the target and the background. Thus, the characteristics observed in Figs. 10 and 11 do not require high spatial

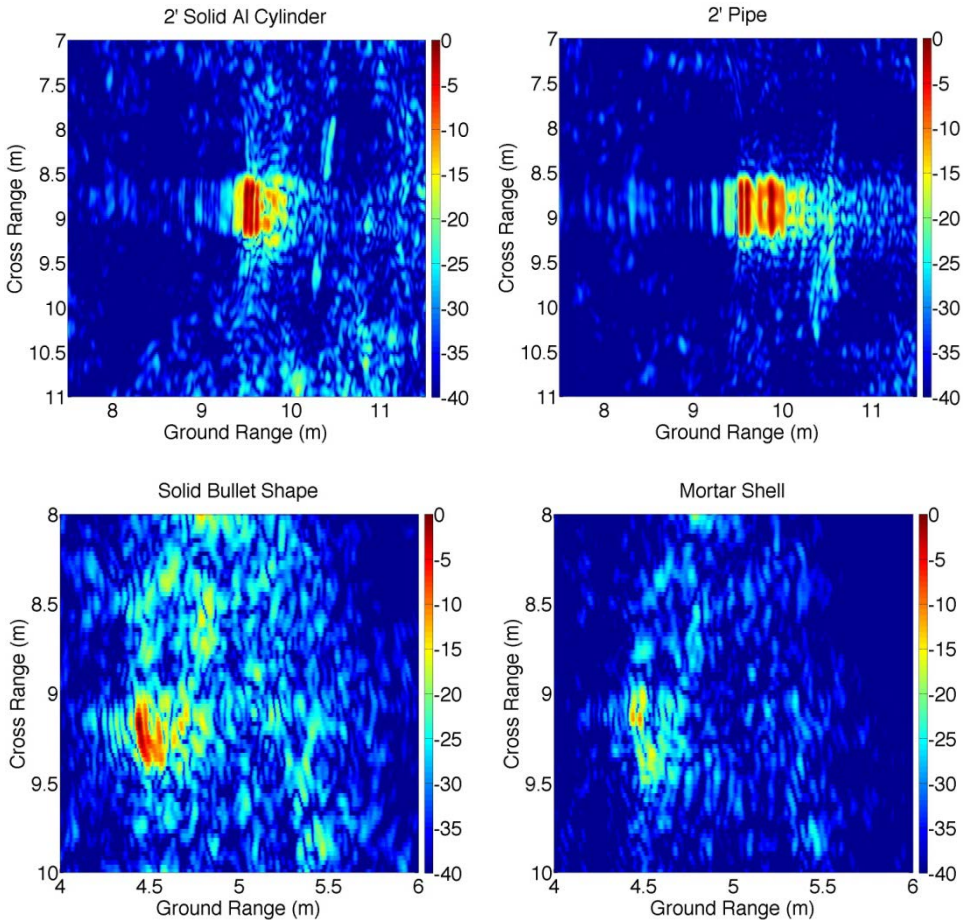


**Figure 9. Backscatter SAS imagery processed from data collected around target broadside at $20^o$ (top images) and $40^o$ grazing angles (bottom images).**

resolution but they can be sensitive to the environment. From the standpoint of classification, it is desirable to project target signals onto spaces that exhibit phenomena unique to the target and that remain robust to changes in the environment. A preliminary look at the issue of environmental sensitivity was addressed with SAS backscatter data collected in 2008 and 2009 and projected onto a target acoustic color space. Measurements on a proud 2ft long x 1ft diameter solid Al cylinder carried out in 2008 were repeated during the 2009 test to test repeatability of the measurements. A comparison of the resulting acoustic color plots is shown in Fig. 12. Clear differences arise in the two cases. Of particular note is the generally weaker end-on response ($90^o$) in 2009 and the apparent loss in 2008 of the elastic cylinder resonance at 6.6kHz and $50^o$ aspect. Preliminary calculations suggest these differences are, at least partially, due to a modification of the interference between the specular echo from the target and the echo that includes a single bounce off the bottom. More simply, in FY 2008, the sand surface behaved more like a soft boundary and, in FY 2009, it behaved more like a hard one due to consolidation, resulting in a phase shift in the reverberant echo component. Additional data collected after the sediment was stirred up by divers using a dredge system (used for target burial) and allowed to resettle, produced an acoustic color plot similar to that obtained in FY 2008.

It is notable that subtle differences in the properties of a sand bottom can lead to fairly significant differences in the acoustic color plot of a target. This comparison emphasizes the care needed

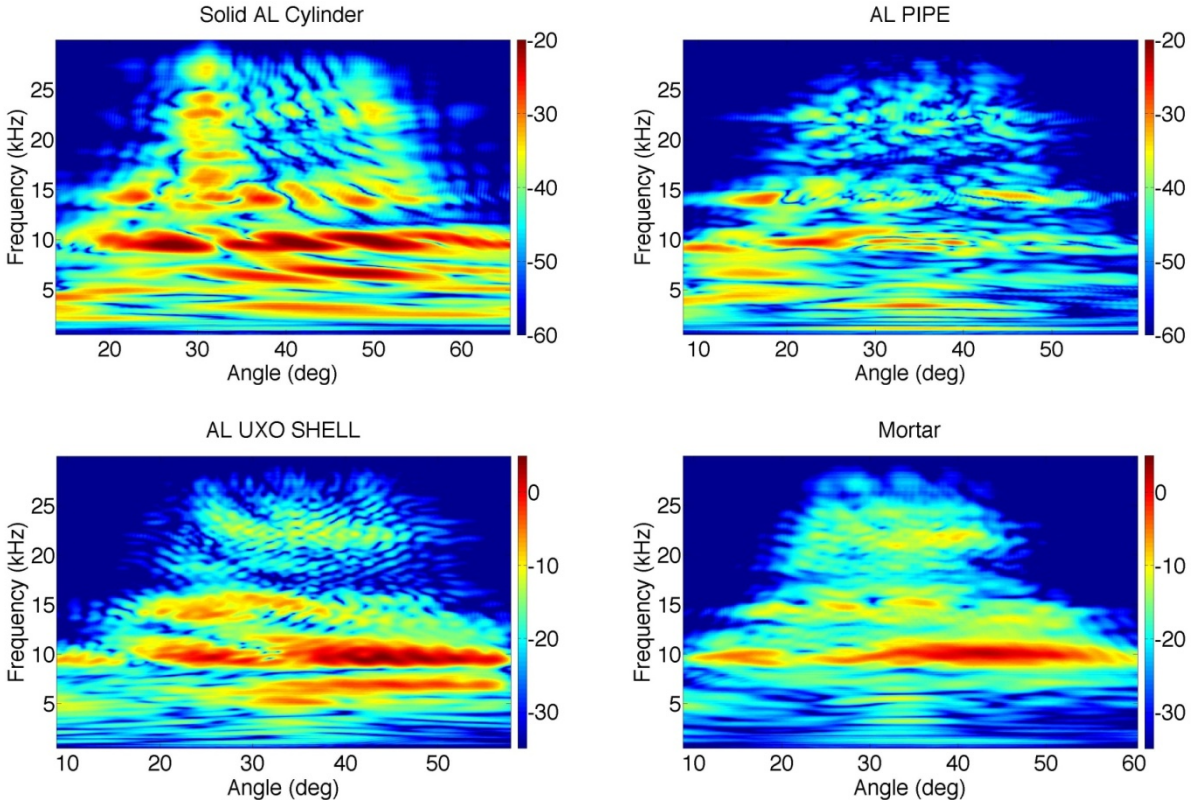


**Figure 10. Backscatter acoustic color processed from data collected around target broadside at $20^o$ (top plots) and $40^o$ grazing angles (bottom plots).**

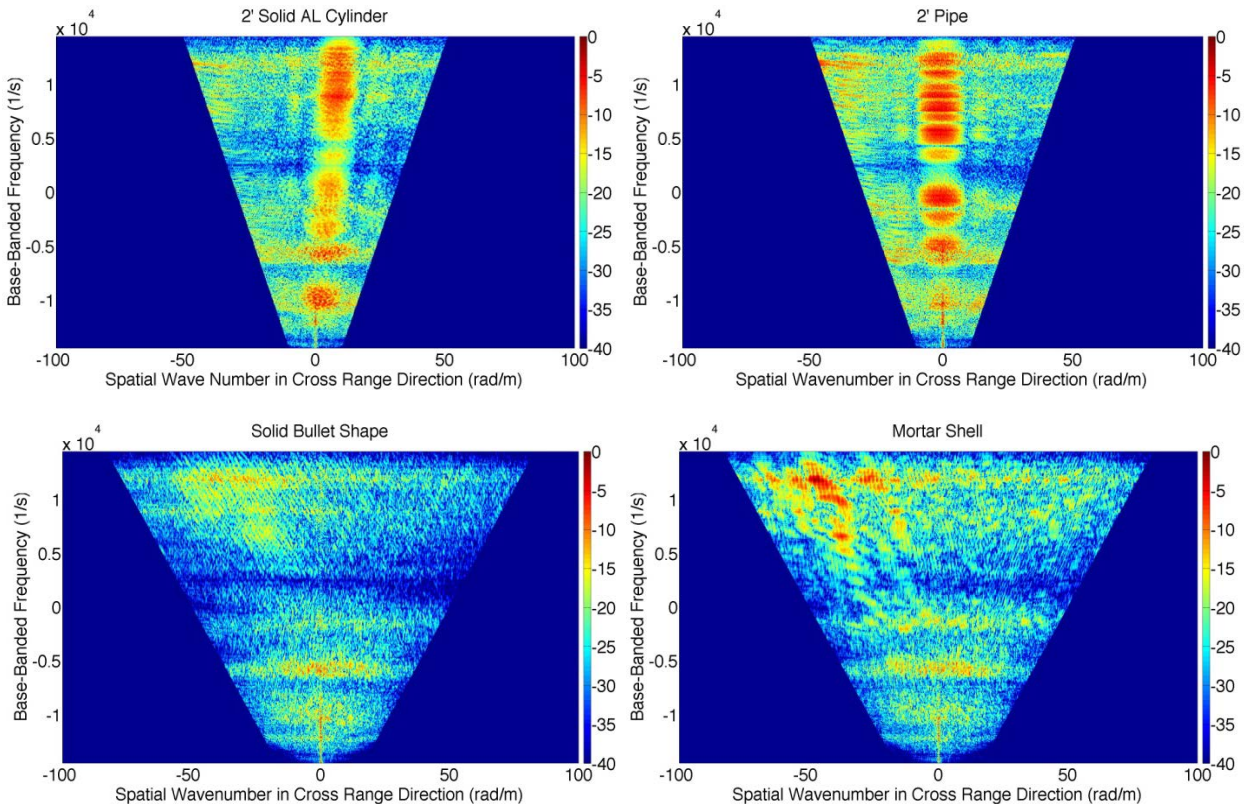


**Figure 11. Backscatter spatial frequency vs frequency plot processed from data collected around target broadside at $20^{o}$ (top plots) and $40^{o}$ grazing angles (bottom plots).**

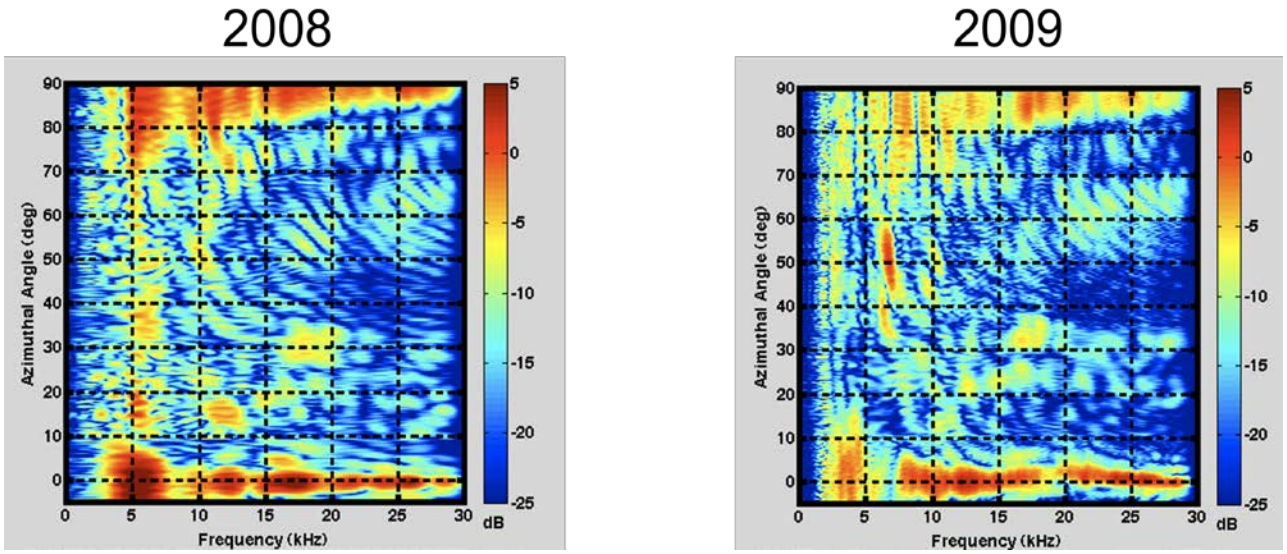


**Figure 12. Comparison of acoustic color for a 2ft long x 1ft diameter solid Al cylinder processed from data collected in 2008 and 2009.**

when preparing data sets for training of statistics-based classification algorithms. A set that exhibits the full range of variation induced by the environments that a target can appear in should be used. Otherwise, in the present case, algorithms trained on 2008 data might not recognize the same target in 2009.

Bistatic UXO scattering data were also collected in 2009-10 and, likewise, a database of these target signals is available for use in ATR-related physics and classification performance studies. Sample data from 2010 using the set-up in of Fig. 5 is shown in Fig. 13, where the NSWC PCD sonar tower projects the signal received at the sonar platform moved along the APL-UW rail. A pulse compressed "smile" for each of the 6 targets listed in Fig. 13 is indicated with red arrows for 5 data collection runs where the axis of each target is arranged proud at the five orientations shown relative to the APL-UW rail. The corresponding SAS beamformed images of the 40$^{o}$ cases over the 30-50kHz band are also shown in the lower right. As might have been expected, compared to the backscatter imagery (not shown) for this target angle, the bistatic imagery exhibits higher SNR due to the more favorable orientation for receiving specular reflections. This indicates some value to bistatic detection which we explored further in 2011 in NSWC PCD's scale-model test tank.

**Tank Measurements:** A c-scan capability was set up in NSWC PCD's scale-model tank to enable simultaneous measurement of monostatic and bistatic target scattering over a continuous range of look angles (J. La Follett, P. Malvoso, R. Lim, NSWC PCD). This facilitated study of the relative advantages of monostatic vs bistatic detection of targets deployed on and under the seafloor.

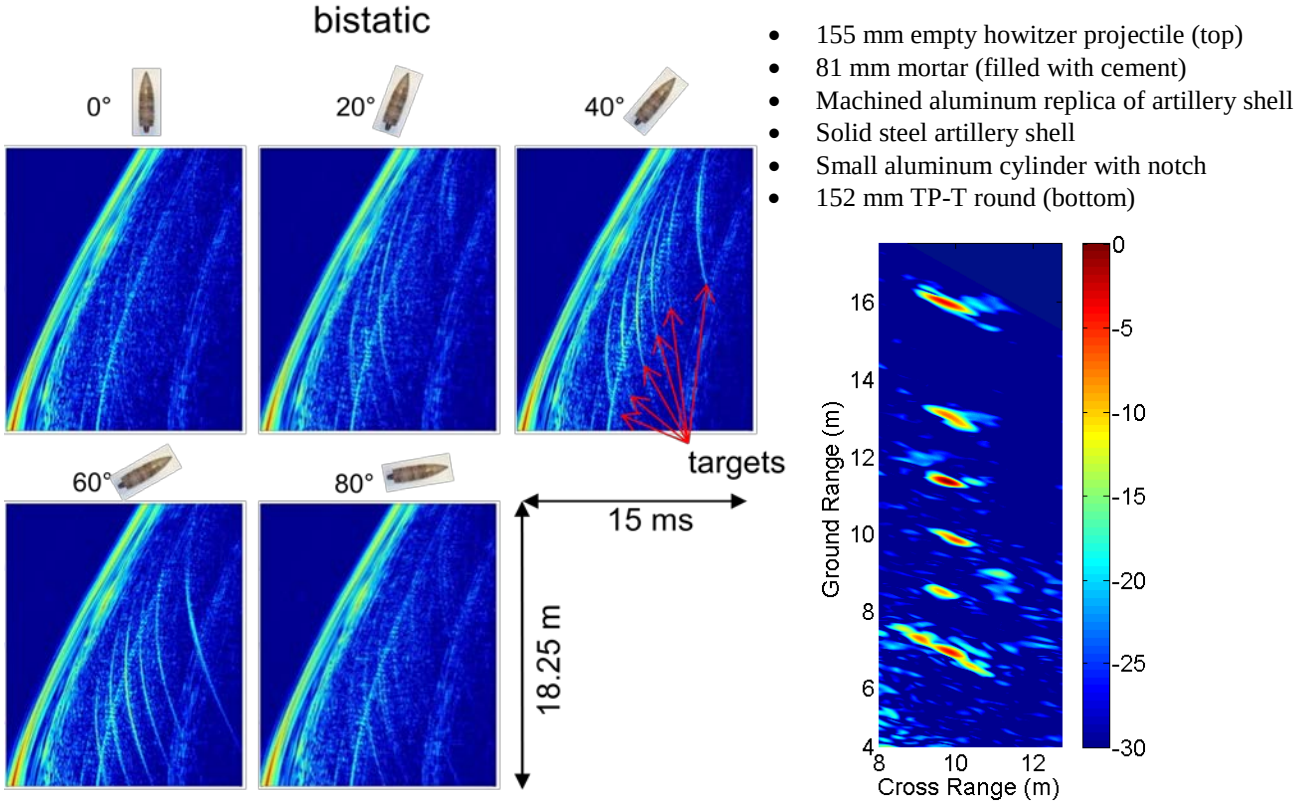


**Figure 13. Bistatic target scattering data (left) and processed imagery (right) from 2010 pond measurements.**

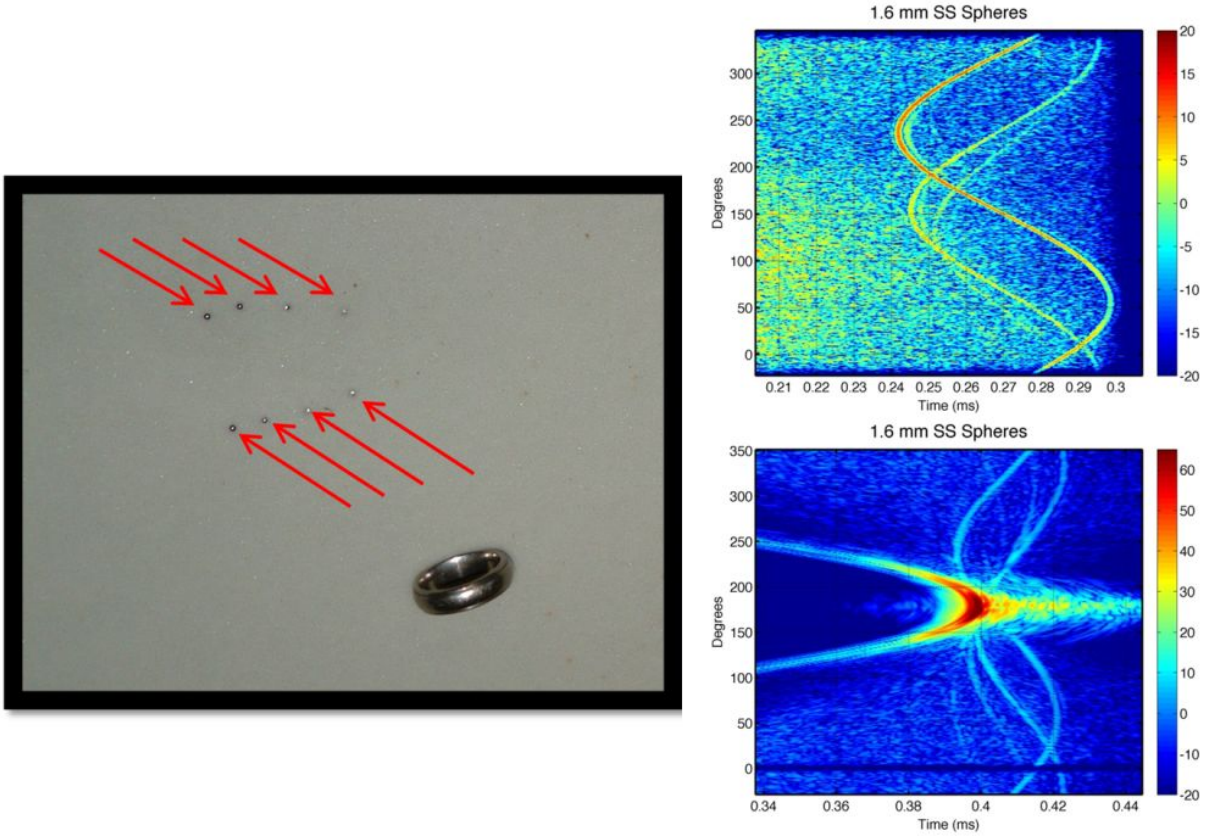


**Figure 14. Picture (left) of 8 stainless steel 1.6 mm diameter spheres (red arrows). There is a ring, not present during the experiment, included in the photo to demonstrate the size of the spheres. Monostatic time-series data (upper right). Bistatic time-series data (lower right). The time-domain data are plotted on a dB scale.**

Results from a scattering measurement are shown in Fig. 14. The source/receiver grazing angle is approximately 6°. The target field consisted of 8 1.6 mm diameter solid stainless steel spheres (***ka*** = 3.5 at the center frequency) in burial states ranging from 10% to 100% buried. The targets are indicated by red arrows (left) and the burial state increases from left to right. The monostatic time series is shown in the upper right. The bistatic time series is shown in the lower right. The brightest bistatic arc is not target related and corresponds to sound that travels directly from the source to the receiver or is reflected once from the sediment. This is also the cause of the very bright region at 180 degrees where the source and bistatic receiver are directly across the circular track and are perfectly aligned. This enhancement is notched out in the time domain before the data can be processed to produce circular SAS (CSAS) images. The phenomena that persist in time after this bright direct-path detection are due to sediment reverberation. Target arcs are evident in both time series plots as sinusoidal curves with relatively smooth amplitudes.

Time-domain beam forming algorithms were developed to process the c-scan data and produce CSAS images. Figure 15 shows the CSAS images resulting from the monostatic (upper right) and bistatic (lower right) time-domain data in Fig. 14. Compared with the bistatic image the monostatic image exhibits higher along track resolution but lower SNR. The lower bistatic

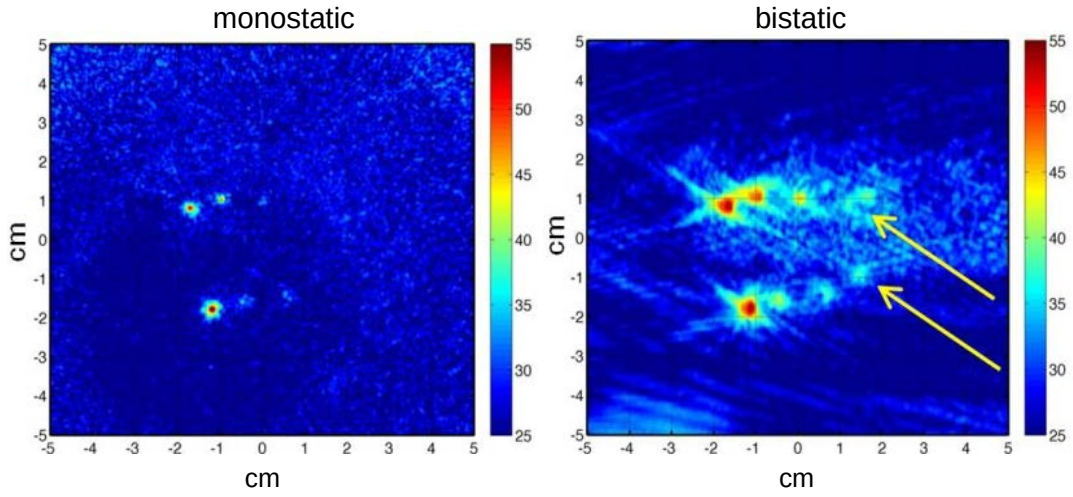


**Figure 15. On the left is the monostatic CSAS image resulting from the upper-right time-domain data in Fig. 14. On the right is the bistatic CSAS image resulting from the lower-right time-domain data in Fig. 14. The data are plotted on a dB scale and the amplitudes have not been corrected to account for the different sensitivities of each receiver. As a result, the absolute amplitudes are not comparable between the two images but relative amplitudes against the background (i.e., SNR) may be compared.**

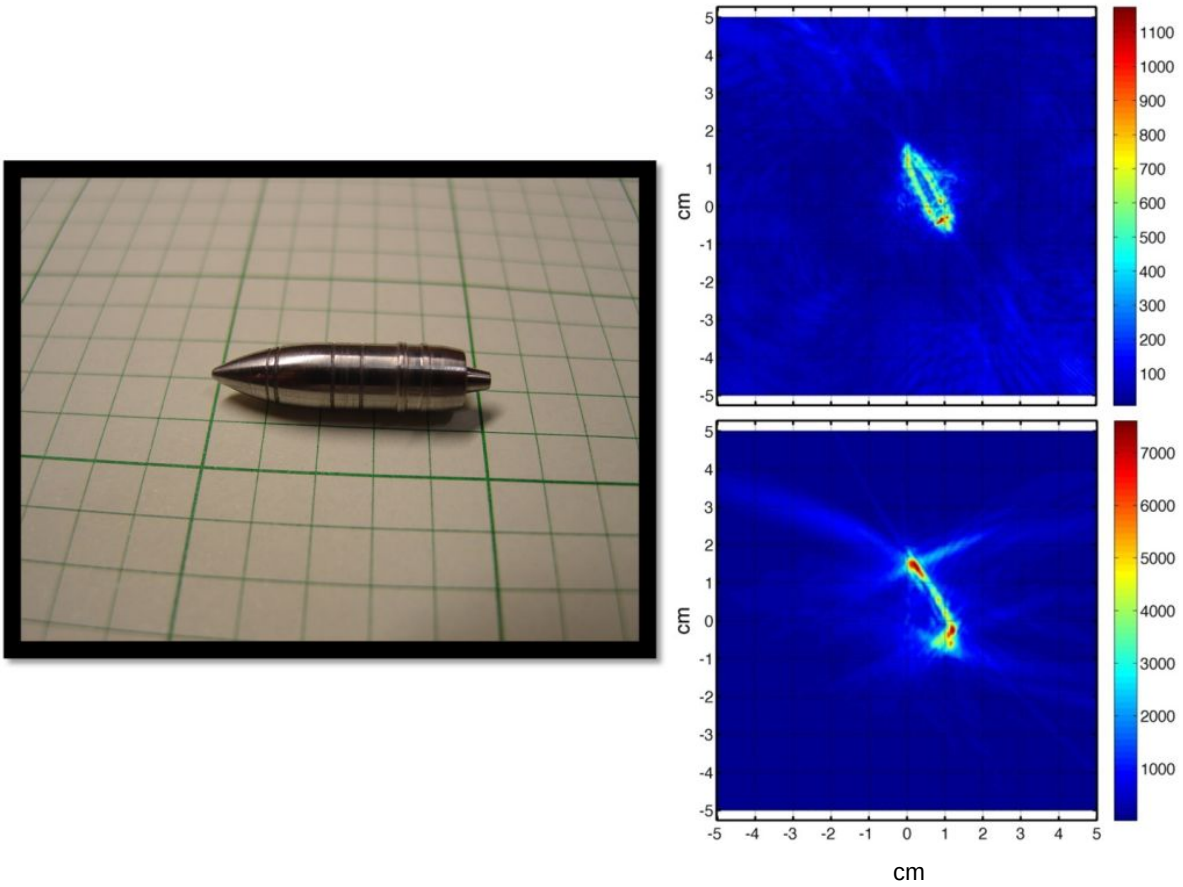


**Figure 16. Picture (left) of 1/16 scale solid Al UXO replica resting on graphing paper with 1 inch large squares (the small squares are .2 inch). Monostatic CSAS image of the UXO resting proud on simulated sediment (upper right). Bistatic CSAS image of the UXO resting proud on simulated sediment (lower right). The data are plotted on a linear scale and the amplitudes have not been corrected to account for the different sensitivities of each receiver. Therefore, the absolute amplitudes are not comparable between the two images.**

resolution is a consequence of the different receiver apertures (the monostatic receiver has a 0.5 mm physical aperture while the bistatic receiver aperture is 19 mm) and/or the moving monostatic source. Target locations in the images are consistent with their actual locations as shown in Fig. 14. Also, the amplitudes of the target images are consistent with the target burial states; the amplitudes decrease from left to right as the burial state increases from approximately proud to fully buried.

Additional examples of CSAS images for proud scaled targets are shown in Figs. 16 and 17. The target shown in Fig. 16 is a 1/16 scale version of the solid aluminum UXO replica used by NSWC PCD and APL-UW in full scale experiments discussed previously at the test pond. Both monostatic (upper right) and bistatic (lower right) CSAS images are shown. As in Fig. 15, the monostatic and bistatic scattering data were obtained simultaneously with one scan. Images corresponding to an identical measurement for a solid 45° aluminum cone having a 19 mm base are shown in Fig. 17. As in Fig. 16, both monostatic (upper right) and bistatic (lower right) images are shown.

Comparing the monostatic and bistatic CSAS images of various targets in Figs. 15 – 17

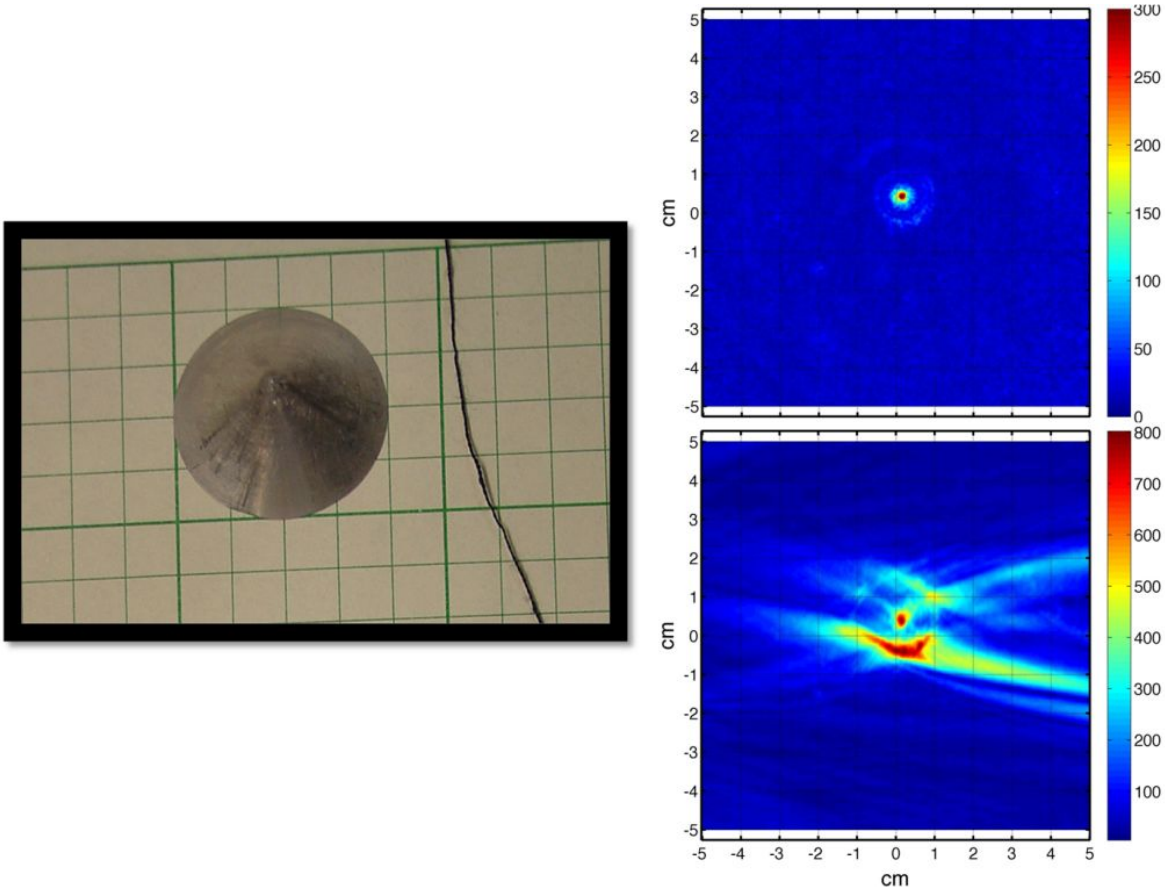


**Figure 17. Picture (left) of .8 inch solid Al cone resting on graphing paper with 1 inch large squares (the small squares are .2 inch). Monostatic CSAS image of the cone resting proud on simulated sediment (upper right). Bistatic CSAS image of the cone resting proud on simulated sediment (lower right). The data are plotted on a linear scale and the amplitudes have not been corrected to account for the different sensitivities of each receiver. As a result, the absolute amplitudes are not comparable between the two images.**

demonstrates some potential advantages for the bistatic geometry. For the target field data in Fig. 15, the two fully buried spheres (far right in the picture) do not appear to be visible in the monostatic image. However, there are bright regions in the bistatic image (yellow arrows) that do seem to correspond to these targets due to the apparent improved signal level, relative to the sediment reverberation, in the bistatic data. The sediment reverberation may be masking the buried target signatures in the monostatic image. For the scaled UXO images in Fig. 16, there are distinct differences. The specular glints from the UXO tip and end dominate in the bistatic configuration and appear stronger relative to the background level than any of the corresponding monostatic returns. The images for the proud solid cone, Fig. 17, show a similar amplitude effect. The bistatic specular reflections dominate the image and provide an outline of the target's base, while the most visible part of the cone in the monostatic image is the tip. Further analysis, accounting for the different receiver sensitivities, needs to be performed to make quantitative comparisons of the amplitudes of the bistatic and monostatic data. However, a distinct advantage of the monostatic CSAS processing for this target is excellent shape rendition, which can aid image-based classification.

Circular bistatic geometries also permit demonstration of several novel bistatic target signatures. Certain elastic target responses have time-domain signatures that arrive earlier than sound following the direct source-receiver path or a path involving one sediment bounce. The time-domain data, for a free-field 1 inch solid stainless steel sphere (***ka*** = 50 at the center frequency), shown in Fig. 18 demonstrate this effect. At an angle of 0° the source is directly across from the receiver, the forward scattering position. At an angle of 180°, or φ = 0° in Fig. 7, the source is positioned between the target and the receiver and there is a resulting drop in received target scattering signal. The timing of the elastic response indicated by a red arrow is consistent with a ray path involving a leaky Rayleigh wave that is launched on the source-side of the target and

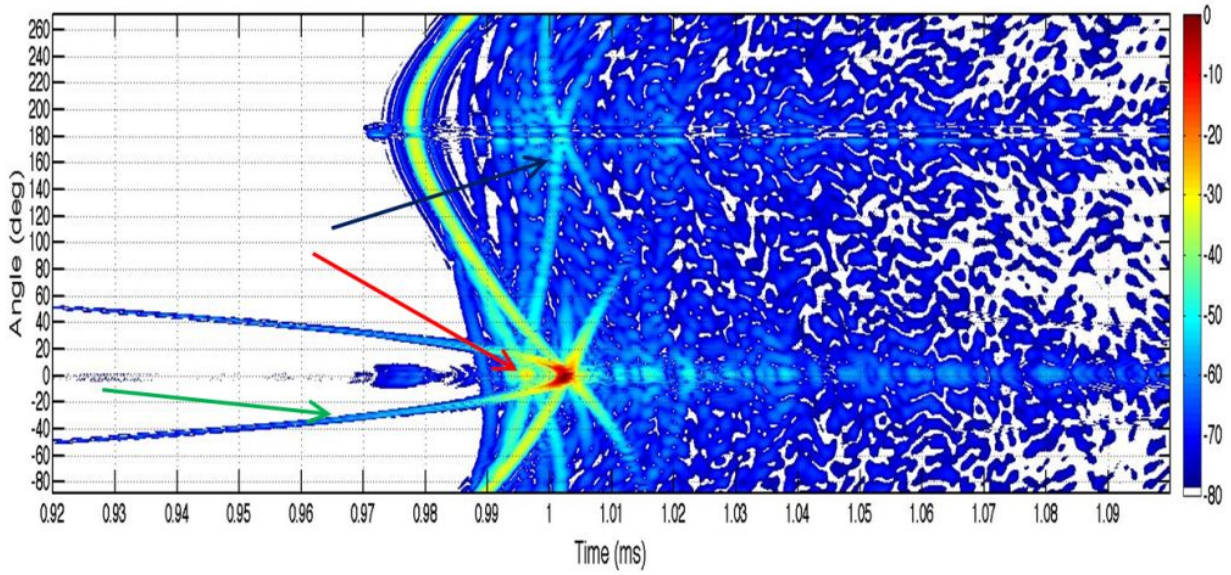


**Figure 18. Bistatic time-series data for a free-field 1 inch diameter solid stainless steel sphere. The source and receiver configuration is shown in Fig. 7 but the angle origin is shifted by 180° from φ. The time-domain data are plotted on a dB scale normalized to the brightest pixel. Backscattering is at an angle of 180 degrees and forward scattering is at 0 degrees. The arc (green arrow) corresponding to sound that travels directly from the source to the receiver has a bright enhancement at 0 degrees when the source and receiver are perfectly aligned. Two elastic responses related to surface waves are indicated by the black and red arrows.**

then detaches on the receiver-side. The surface wave travels with a phase velocity roughly twice that of the surrounding fluid, $C_R$ = 2.97 mm/μs. As a result, the surface wave segment of the ray path causes the disturbance to arrive 5.7 μs before sound that travels directly from the source to the receiver without interacting with the target. The black arrow indicates a backscattering enhancement that is also related to high-frequency surface waves.

The monostatic/bistatic configuration shown in Figure 19 (left) was used to demonstrate novel bistatic target signatures in free-field for a 5:1 solid aluminum cylinder with flat ends. This configuration permits simultaneous measurement of the backscattering and direct forward scattering as a function of target aspect angle. In the forward scattering time series (lower-right), there are two "half-moon" shapes at 0° and 180° (red arrows). The first of these

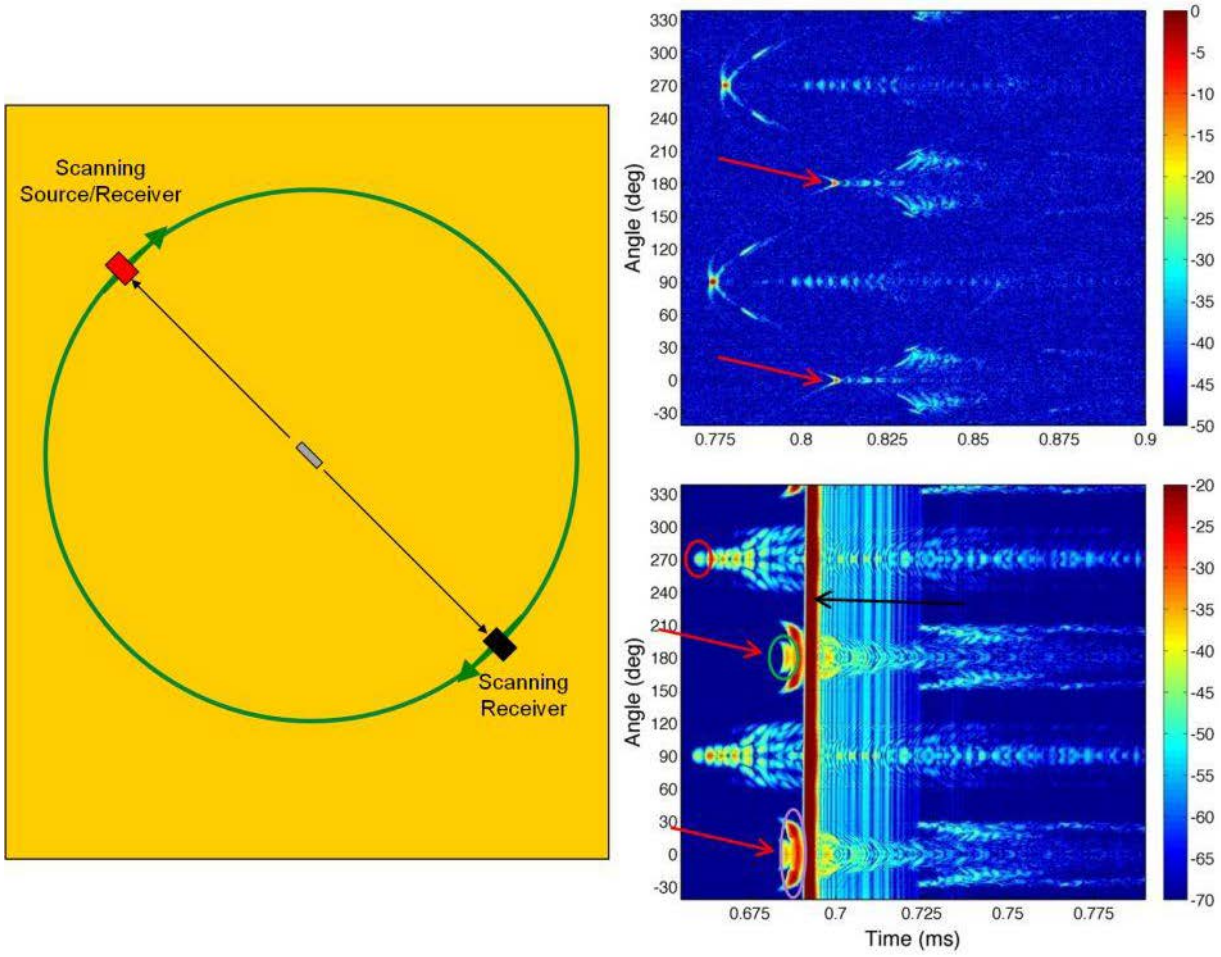


**Figure 19. Diagram (left) of the circular-scan setup for free-field target measurements having a monostatic source/receiver with a bistatic receiver mounted directly across the circular scan line. Both the source/receiver and the bistatic receiver are translated on a circular path simultaneously, while keeping their relative positions fixed. The bright vertical lines (black arrow) are not target related. They are the result of sound traveling directly from the source to the receiver. A stationary 5:1 .5 inch diameter solid aluminum cylinder is suspended in the center of rotation. The backscattering time-series data (upper right) and the forward scattering time-series data (lower right) are plotted as a function of aspect angle. The time-domain data are plotted with a 50 dB dynamic range and normalized to the brightest pixel in each plot. At angles of 0 and 180 degrees (red arrows) the source is broadside to the target.**

(green oval) extends from roughly 166° to 194°. This angle range is consistent with the cutoff angle of 13.5° for transmission of sound from water into a longitudinal wave with $C_L$ = 6.41 mm/μs. The artifact vanishes as the angle of incidence is increased beyond that value. This behavior is symmetric about broadside, as expected. At broadside, the timing is also consistent with a longitudinal wave that is transmitted though the side of the cylinder. For a 12.7 mm diameter cylinder at broadside, this type of elastic response would arrive 6.5 μs before the direct path, which is in agreement with the observed timing difference to within 0.5 μs.

Similarly, the broader artifact (purple oval) that arrives next in the time series, Fig. 19 (lower right), is consistent with a transmitted shear wave where $C_s$ = 3.17 mm/μs. The corresponding cutoff angle is 28.1°. This is in agreement with the angle range of roughly ± 30° evident in Fig. 19 (purple oval). The timing is also consistent with a shear wave that is transmitted though the side of the cylinder. For a 12.7 mm diameter cylinder at broadside, this type of elastic response would arrive 4.5 μs before the direct path and that is in agreement with the observed timing difference to within 0.5 μs.

Finally, there are also elastic responses at angles of 90° and 270° that arrive before the sound that travels directly to the receiver. The arrival time of the earliest artifact (red circle) is consistent with a ray having an elastic wave segment that travels the 2.5 inch length of the cylinder at the bar velocity $C_B$ = 5.1 mm/μs. This gives an arrival time of 30.2 μs before the direct path which is within 2.5 μs of the signal observed in the time series.

The backscattering and forward scattering time-domain data in Fig. 19 can be normalized by the incident pulse, accounting for spherical spreading, to calculate the target strength as a function of aspect angle (acoustic color) shown in Fig. 20 (right). There is a vertical notch (black arrow) evident in the forward scattering time series (lower left) where the strongest portion of the direct path has been removed in order to isolate the forward target scattering in the target strength calculation.

The forward scattered target signatures in Figs. 19 and 20 have potential advantages for both target detection and classification. The bright broadside signals (red and purple ovals) are less directional than the broadside monostatic specular reflection. As a result, they are present for a significantly larger range of angles. The corresponding phenomena in the target strength see Fig. 20 (lower right), have comparable amplitudes to the broadside specular result. Specular reflections that dominate backscatter signals are also largely characteristic of the source while the forward-scattered signals are associated with an elastic response characteristic of the target. Therefore, these signals should be more suitable for extracting features for non-image-based classification analysis if they can be separated from the source signal. The rich structure in the forward scattering target strength (forward scattering acoustic color) in Fig. 20 demonstrates this possibility in the free-field case. Although the forward scattered signals discussed here are seen in free-field in the plane of the source and receiver, their angular width and their physical origin suggests they may be observable also for elongated metallic targets deployed on the ocean floor and detected at shallow angles in a forward scattering configuration.

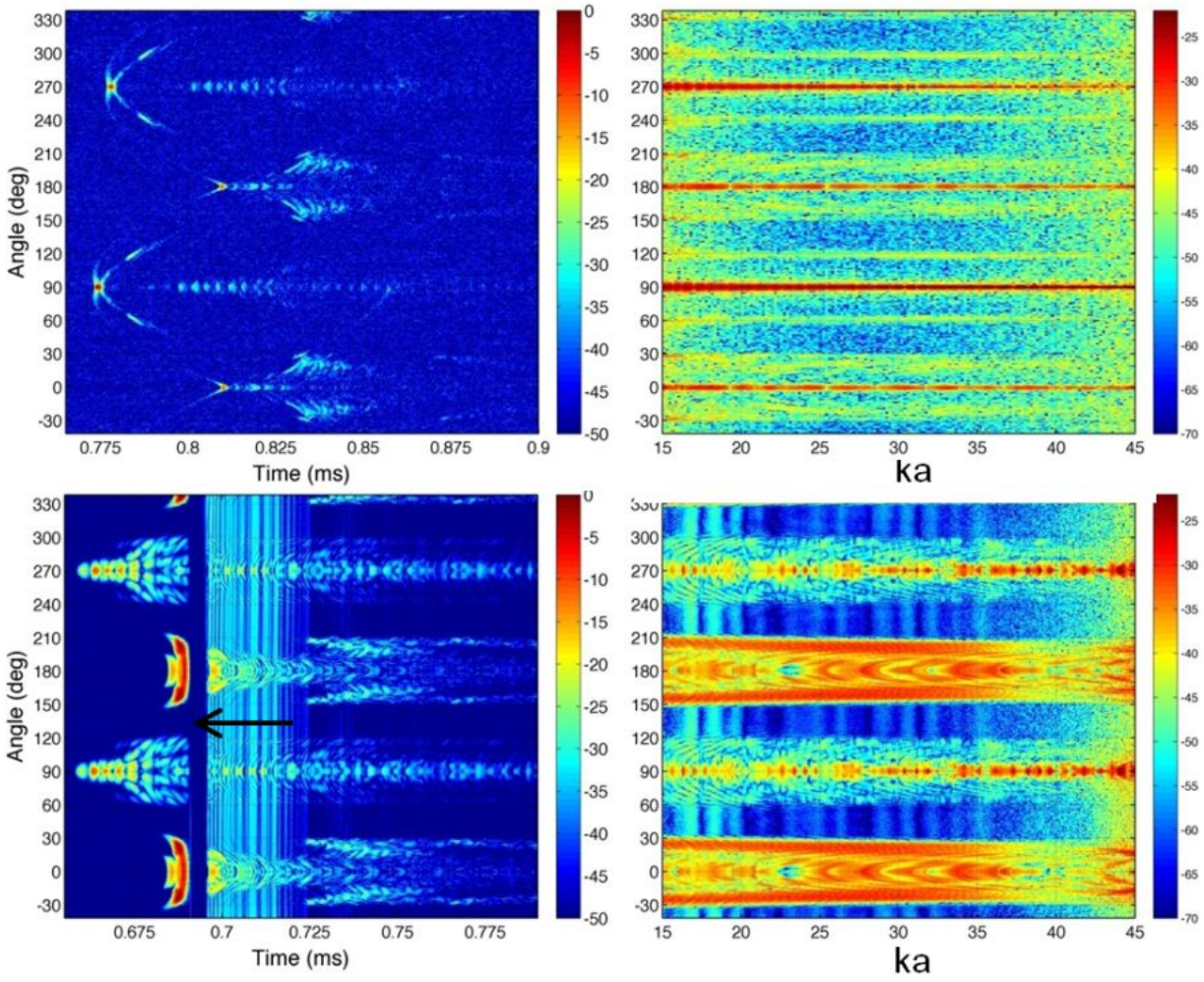


**Figure 20. Time-domain free-field data for backscattering (upper left) and forward scattering (lower left). Target strength for backscattering (upper right) and forward scattering (lower right). A stationary 5:1 .5 inch diameter solid aluminum cylinder is suspended in the center of rotation. The time-domain data are plotted with a 50 dB dynamic range and normalized to the brightest pixel in each plot. For the forward scattering target strength (lower right), the direct source-to-receiver pulse was notched out in the time domain data (lower left). The vertical null in the data caused by this notch is indicated with a black arrow.**

**Data/model comparisons validating test tank results:** The question of whether collecting data in NSWC PCDs small-scale test tank introduces any anomalous artifacts was addressed by comparing to T-matrix simulations. To facilitate comparisons with T-matrix predictions, a measurement was performed for a 2.4 mm diameter solid stainless steel sphere resting proud on the scaled simulated sediment. The time-domain bistatic scattering data are shown in Fig. 21 (left). The source and receiver grazing angles were 8.8° and 5.2°, respectively. The source/receiver scan configuration is shown in Fig. 7 (where the angle axis has been shifted by 180° from φ) and the center frequency was .55 MHz. As in Fig. 18, at angles of 0° and 360° the source is directly across from the receiver, the forward scattering configuration. At an angle of 180° the source is positioned between the target and the receiver (backscattering position) and

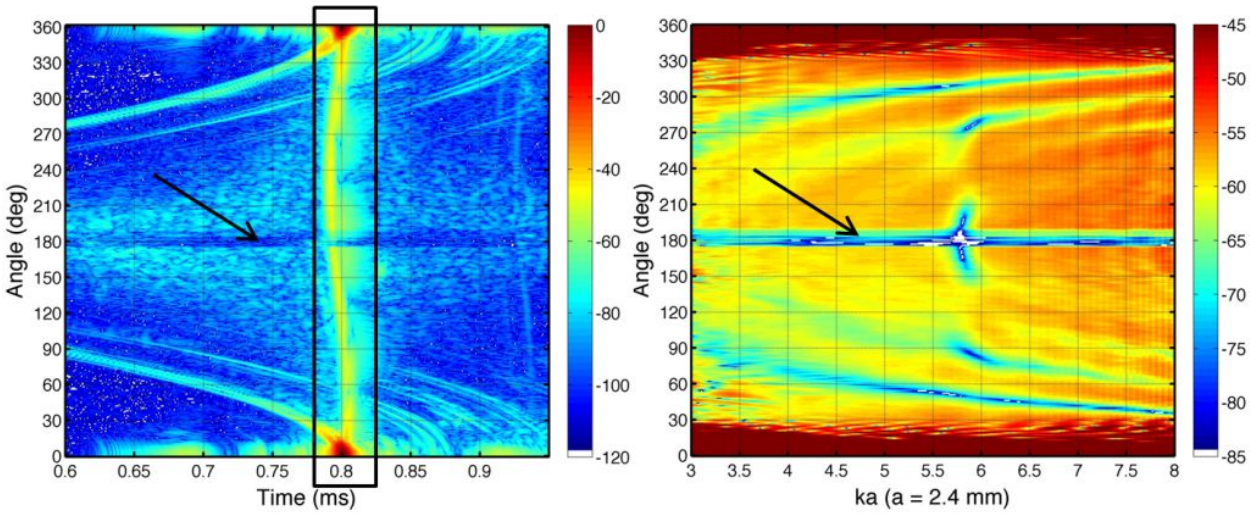


**Figure 21. Time-domain bistatic scattering data (left) for a proud 2.4 mm solid stainless steel sphere plotted on a dB scale normalized to the brightest pixel. Bistatic target strength (right) from a windowed subset (black rectangle) of the time-domain data isolating the target scattering. The horizontal null (black arrows) in both plots is caused by the source blocking the receiver at 180° (backscattering), see Fig. 7 at φ = 0°.**

there is a resulting drop in received target scattering signal. A subset of this data containing the target scattering is windowed in time (black rectangle) and then normalized by the incident pulse amplitude in the frequency domain. Then, after compensating for spherical spreading, we arrive at the target strength as a function of bistatic scattering angle shown in Fig. 21 (right).

A notable asymmetry above and below $180^o$ is seen in both the windowed time domain signals and the target strength plot. For a perfectly centered sphere, both of these should be symmetric. The sinusoidal curvature of the arrival times of the target scatter seen in the left of Fig. 21 is caused by a sphere that is not perfectly centered. Since this imperfect centering was not corrected by time shifting the data before windowing the target signals to generate the target strength plot, a corresponding asymmetry was transferred to the target strength plot because the signals windowed below $180^o$ appear to include more of the bottom reverberation noise that arrived before the target specular and less of the desired target reradiation after the specular.

The T-matrix model prediction for the target strength in Fig. 21 is shown in Fig. 22 (left). Model acoustic inputs came from measurements of the sediment properties (sound speed and attenuation) and tabulated values for the target compressional speed. The target shear speed was found by fitting resonance features sensitive to the shear speed in measured and predicted free-field form functions. The plot in Fig. 22 shows the measured target strength of the proud sphere for comparison. The amplitudes are plotted on a dB scale with a 40 dB range. The angle, amplitude, and ***ka*** ranges are the same in both plots; however the measured target strength (right) is shifted by -5 dB relative to the simulation result (left). This discrepancy is believed to be due to differences in the normalization procedure between measurement and simulation. At angles near 0° and 360° comparisons are not valid since the measured data contain the direct path from the source to the receiver, while the simulation results are for target scattering alone. Otherwise, per the discussion regarding the asymmetry of the target strength from measured data, it is noted

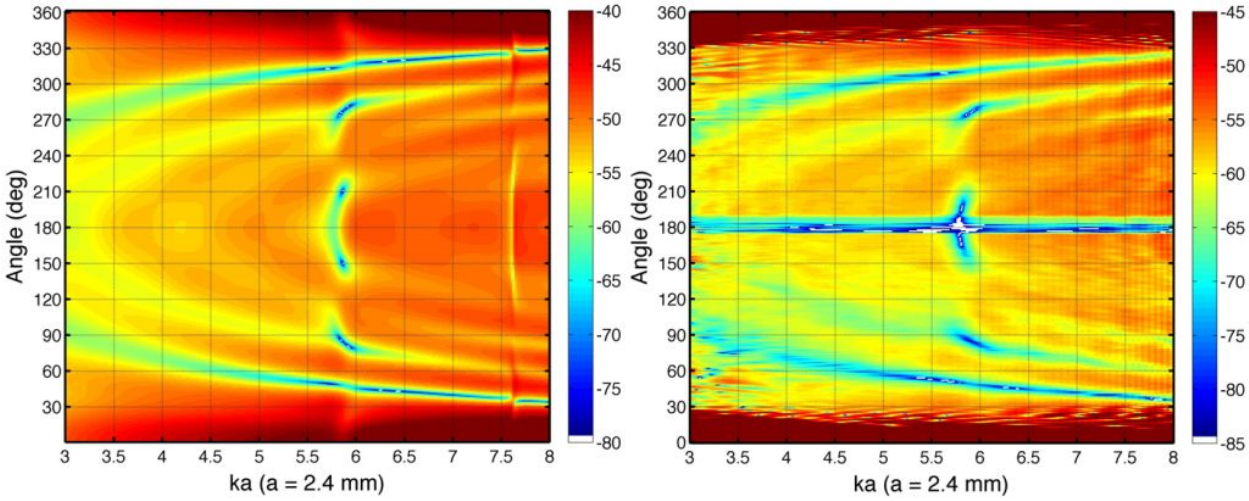


**Figure 22. T-matrix simulation model predictions for the target strength (left). Measured bistatic target strength (right).**

that the results above 180$^{o}$ are reasonably close to the T-matrix simulation, as expected. Aside from structure that is masked by the bottom bounce, the data reproduces most of the structure observed in the model but degraded by a reasonable level of bottom reverberation noise. Spurious effects from walls and experimental hardware are understood and controllable. This demonstrates the tank data can be used to realistically represent target and environment interactions.

**FE development and modeling:** The development of a FE capability for UXO sonar simulations is proceeding towards maturity with several checks of the fidelity of calculations having been performed for canonical target shapes on a sand bottom (D. Burnett, R. Lim, NSWC PCD). Due to the envisioned complexity of real targets, a considerable effort was made to formulate efficient meshes for shelled structures interacting with an ocean interface like the seafloor. Mesh refinements were formulated to automatically maintain only the calculation load needed to maintain a nominally uniform error across a wide frequency band. Some of these refinements are illustrated in Fig. 23 for one of the benchmark comparisons using a spherical shell.

Verification of these refinements for scattering by a 5%-thick, stainless-steel, spherical shell insonified at high (40$^{o}$) and low (20$^{o}$) grazing angles under proud, half-buried, and buried configurations is demonstrated in Fig. 24. Although verification studies must be carried out using simple targets because high-accuracy benchmark solutions of the underlying linear acoustic equation are required, the refinements imposed on the FE solution of these targets are expected to be effective for all targets.

Validation of the underlying linear acoustic equations solved with the FE solution engine in COMSOL was also checked by comparing the computed target strength acoustic color of a solid Al cylinder of 5:1 aspect ratio with carefully controlled free-field measurements provided by WSU (P. Marston and K. Baik). This is shown in Fig. 25. Agreement is seen to be very good with some small discrepancies that can be attributed to limits on what can be controlled in the

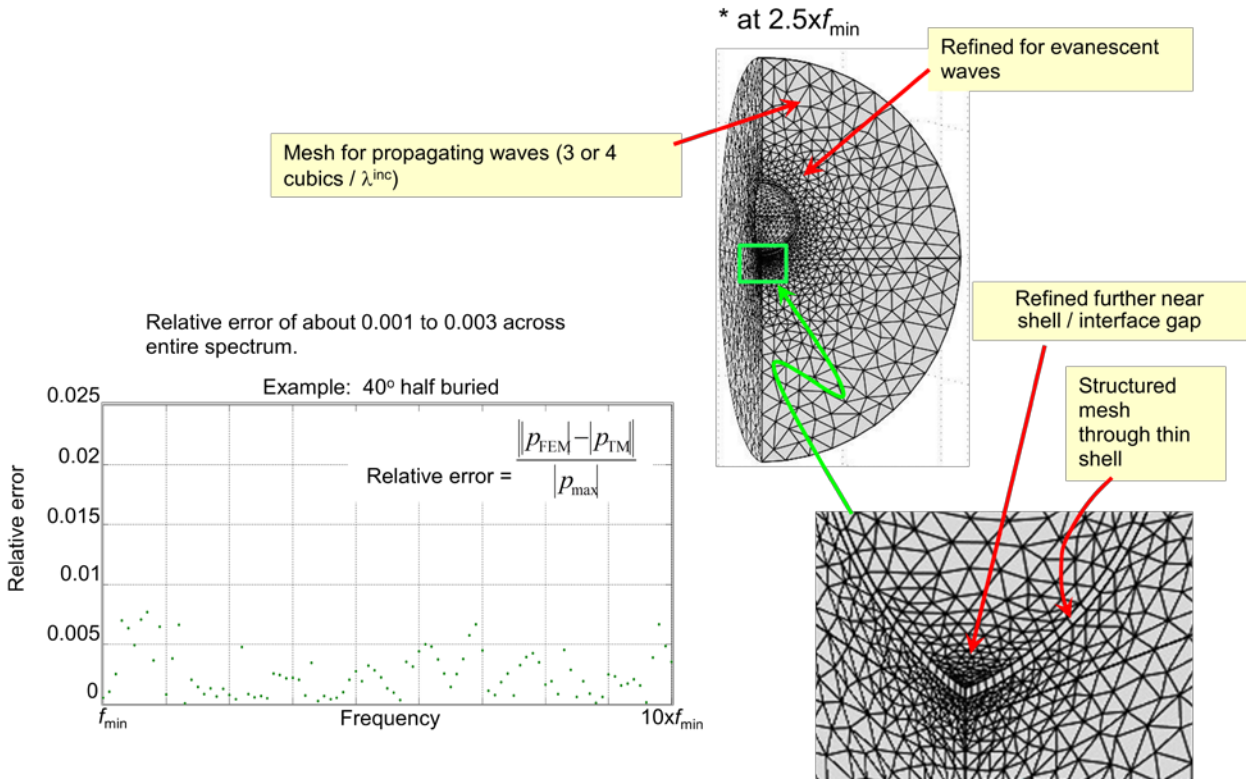


**Figure 23. Mesh refinements formulated for scattering by a proud spherical shell.**

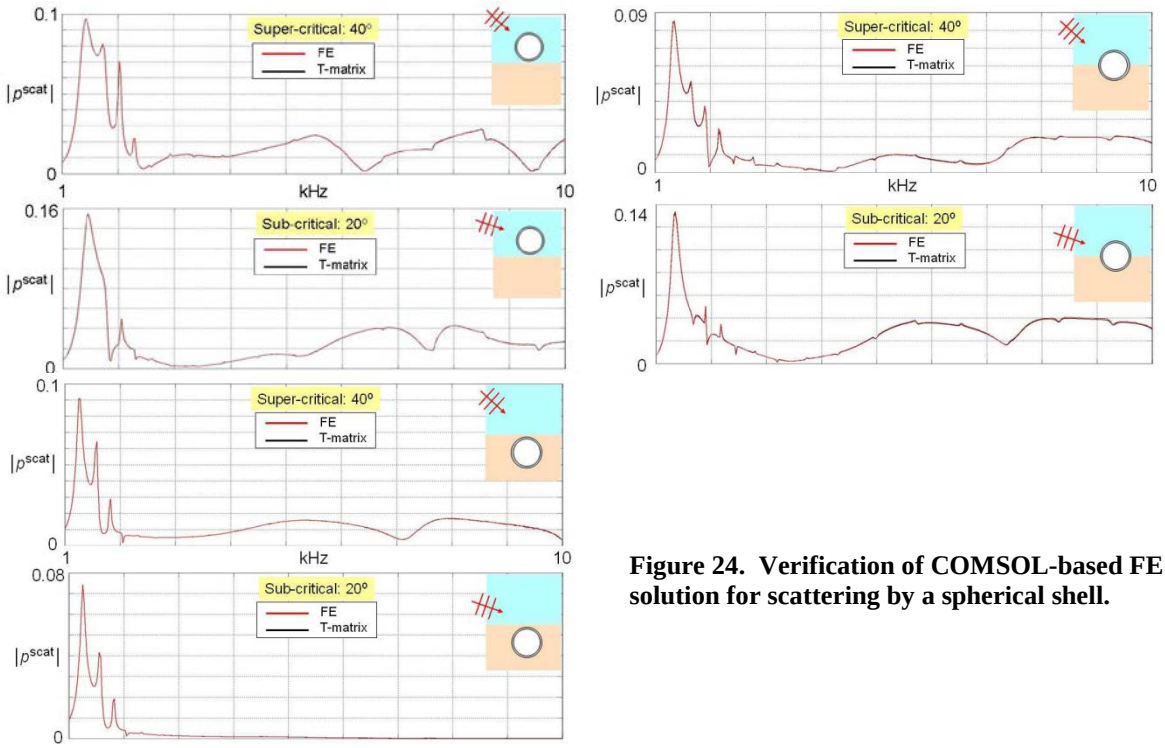


**Figure 24. Verification of COMSOL-based FE solution for scattering by a spherical shell.**

measurements: e.g., not having the exact material parameters for the Al cylinder as FE inputs, small variations in uniformity of the material properties of the target, limited experimental SNR, or lower measurement resolution than produced in the FE computation. Lower measurement resolution can be the result of limited tank size, which limits the amount of raw time-domain signal that can be collected before contaminating wall reverberation appears. Nonetheless, the range of agreement seen here is likely the best that can be expected when comparing with measurements.

As the FE capability continues to mature, it is being applied to help interpret observations of scattering by bottom targets. In Ref. (4), FE simulations were used to elucidate environmental effects observed on scattering by a proud Al cylinder on a sand bottom. Figure 26 compares the FE computed target strength in acoustic color space with measured values from 2009 in the NSWC PCD pond (right-hand side of Fig. 12) using the measured sand parameters appropriate for an assumed fluid bottom. Here, the differences were initially thought to be due to neglecting the shear elasticity of the bottom in the FE calculation since the sand was reported to be compacted and hard by divers. Since no shear speed measurements of the sand bottom were possible during the test, the measurement could not be modeled with this bottom property included. However, FE calculations allowing shear speeds in the bottom did not produce the phase shift needed in the surface reflection coefficient to reproduce the observed differences unless the shear speed was chosen outside a realistic range. Resolution of these differences remain under investigation.

In 2011, FE simulations proceeded to more complex targets and target orientations requiring 3-dimensional (3D) modeling with a systematic focus on developing efficient solutions with controlled accuracy. This included testing and resolving problems in software updates used to transport simulations to a 25 processor rack computer. Simulations on an air-backed cylinder both in free-field and in various configurations on a sand bottom have been completed. These will be used in tests of classification algorithms under development.

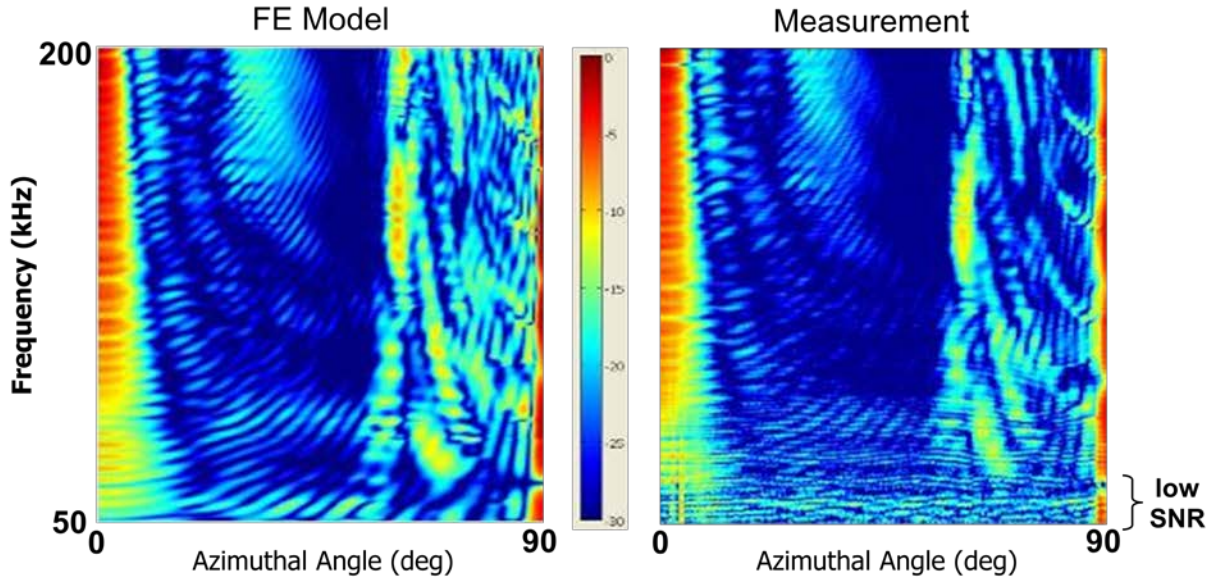


**Figure 25. Validation of COMSOL-based FE solution for scattering by a free-field 5:1 solid Al cylinder.**

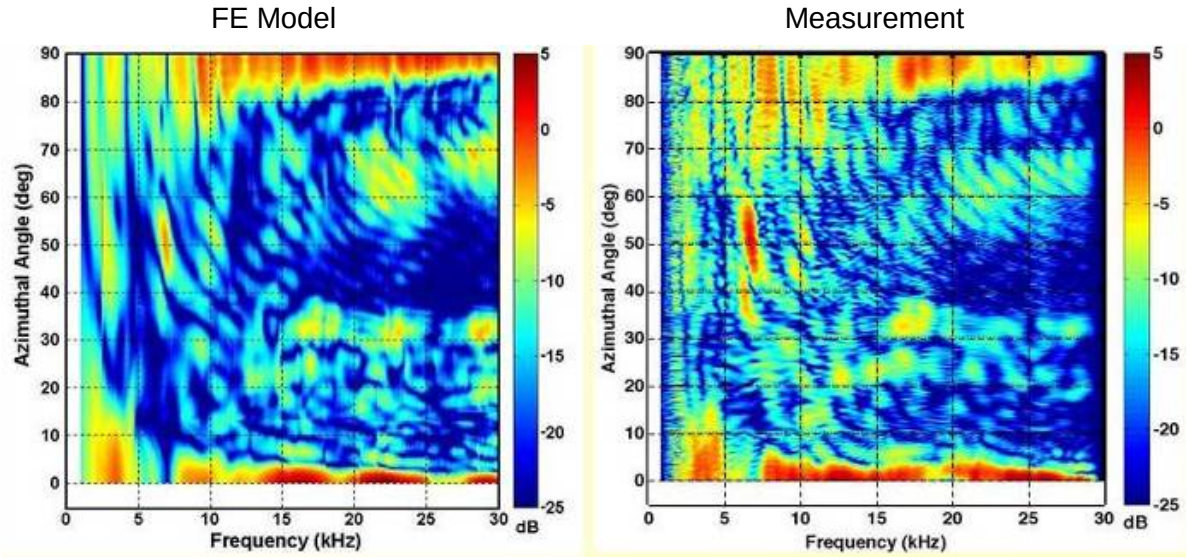


**Figure 26. FE vs measurement comparison for scattering by a 5:1 solid Al cylinder deployed proud on the sand bottom of the NSWC PCD freshwater pond.**

Other 3D simulations concentrated on targets deployed in NSWC PCD's pond in 2010 to help interpret the data collected. For example, the "paddle" target deployed by WSU (see the notched Al cylinder in Fig. 5 photo) was meant to investigate the potential for exciting torsional elastic modes that may be unique to many elongated, finned UXO. In Fig. 27, a comparison of FE generated and measured backscatter target strength plots are shown for this target in free-field. Here, the paddle is face up and the source and receiver are in the plane of the paddle axis. Data was simulated and collected with the paddle rotated 360$^{o}$ around an axis perpendicular to the paddle axis. This is illustrated in Fig. 28. Per the scattering configuration depicted, plots should

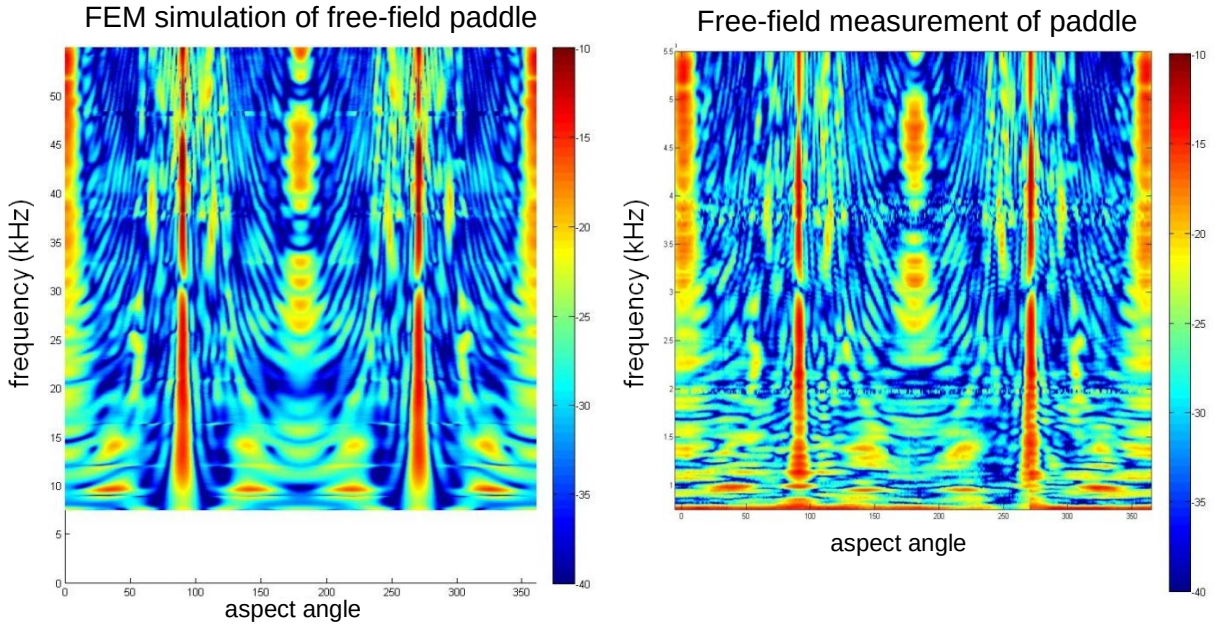


**Figure 27. Comparison of FE simulated and measured free-field target strength plots for WSU's "paddle."**

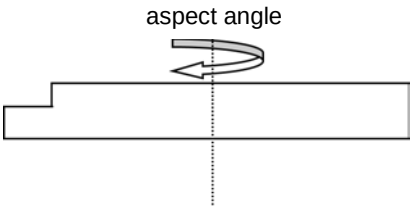


**Figure 28. The orientation of the paddle for data generated and collected for Fig. 27. The source field is incident into the page and 0° aspect = broadside.**

be symmetric around 180°. The agreement between both plots is good but the measured result exhibits a more ragged appearance, especially at lower frequencies, that makes the expected symmetry less perfect and is attributed to unavoidable noise contamination. Backscatter FE simulations and measurements for the paddle spun around its longitudinal axis in free-field and deployed on the bottom of NSWC PCD's pond have also been compared and these results are being studied further with WSU to understand phenomena observed in the target strength plots.

3D FE simulations of the solid bullet shaped UXO (see the Al artillery shell replica in Fig. 5 photo) were also run for comparison with pond measurements as well as with 2D FE simulations generated by APL-UW. Even though targets deployed on a sand bottom would require 3D modeling to rigorously account for all wave effects, the comparisons showed that 2D FE simulations that include only a couple of the bottom bounce interactions with the target will capture most of the backscatter response, at least, if the target is axially symmetric and multiple scattering with the bottom is weak. This type of 2D modeling was utilized in the analysis of the Al cylinder of Ref. 4 and a similar result was found here for the UXO. Simplifications to the FE modeling such as these can be valuable for speeding up generation of target databases but the degree to which it can be extended remain to be quantified. While unsymmetric UXO are not expected to be well modeled with 2D FE, more cases involving axially symmetric UXO like the sample tilted case computed with 3D FE shown in Fig.29 will be checked in ongoing work.

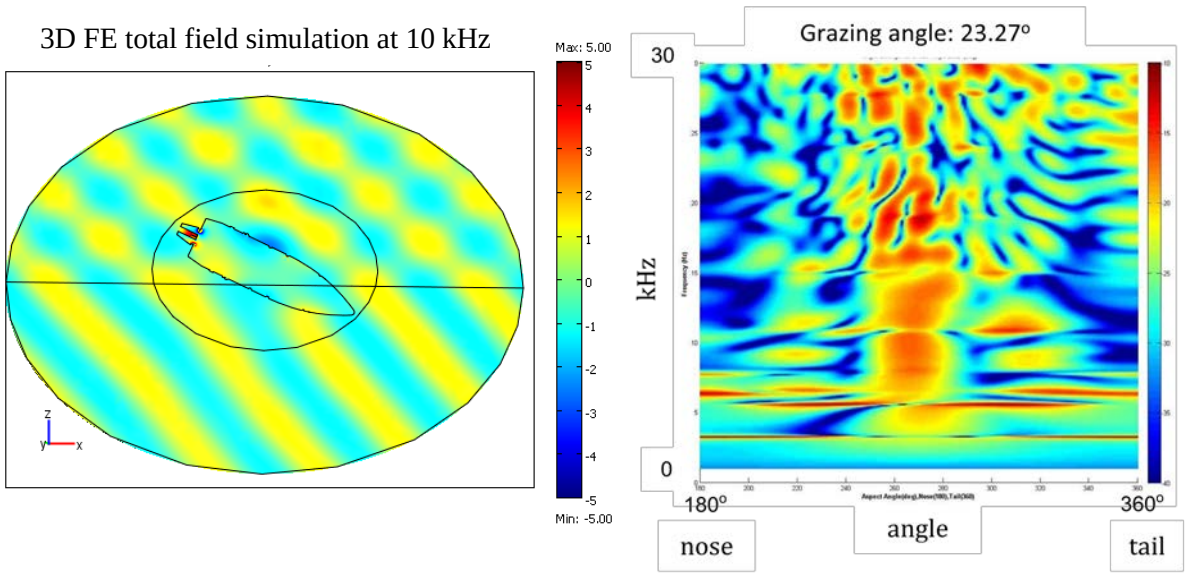


**Figure 29. 3D FE simulation of scattering by artillery shell embedded in a sand bottom with a 25° tilt. Plots of total field (left) and backscatter target strength vs. frequency and aspect angle (right) are shown for a plane wave incident at a 23.27° grazing angle.**

**Classification analysis:** In addition to capturing data on targets to train and test classifiers, ways to ensure enough data is captured to produce robust classification were developed. One of these methods imbeds new targets into imagery from past surveys in different environments (G. Sammelmann, NSWC PCD). This is done by importing actual images from a given sonar system into PC SWAT, where the image is normalized and a reflectivity map is created as a function of the x and y coordinates of a point on the bottom. This reflectivity map is used to normalize the direct path bottom reverberation computed by PC SWAT. This procedure allows PC SWAT to compute the raw stave data needed to reproduce the original image in addition to other noise sources and targets.

Because phase information is not known from the original image, this process does not ensure the targets are imbedded into the same bathymetry in the originally surveyed area but it is a more realistic way to combine environmental effects with target signals than adding randomly generated band-limited noise. The user can imbed an arbitrary target into an existing image with minimal artifacts and reverberant reflections from the target and bottom are consistently phased in the raw data. Absolute scattering levels from the original survey are also not known so the relative level is chosen to produce a realistic overall SNR. Target signals collected in other tests or simulated with tools such as FE can also be appropriately scaled and summed into data reconstructed from the reflectivity maps to create new data sets. This method is illustrated in Fig. 30

.

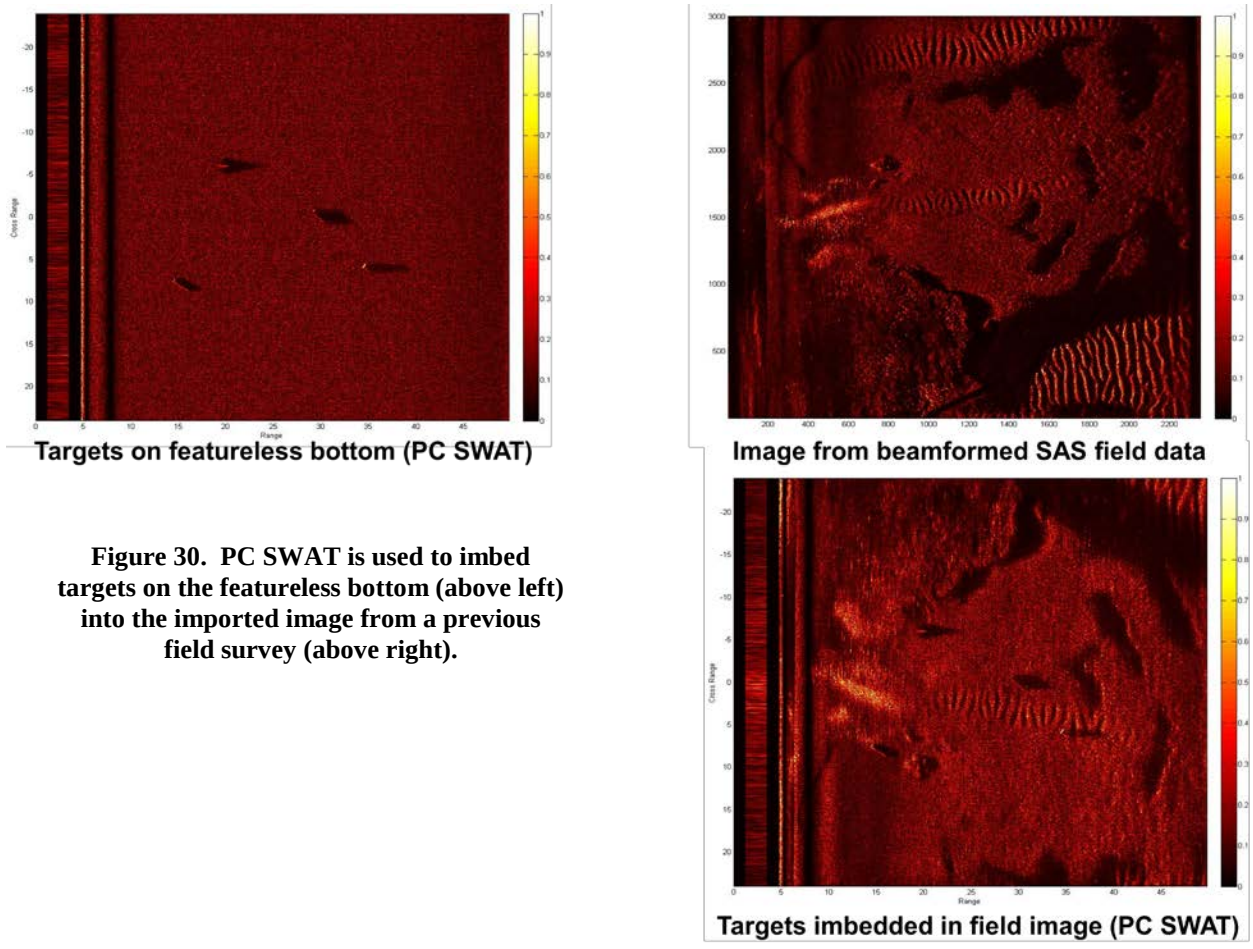


**Figure 30. PC SWAT is used to imbed targets on the featureless bottom (above left) into the imported image from a previous field survey (above right).**

Another way to capture more data for ATR use is to make data collection more efficient. Toward this end, an algorithm was written in MATLAB (T. Marston, NSWC PCD) to allow efficient isolation of target signals for subsequent processing into other target representations; e.g., acoustic color. Figure 31 illustrates the technique. The algorithm beamforms raw SAS data to image a limited range interval where multiple targets appear, so that signals associated with a target of interest can be isolated by cropping out the others in image space. The isolated image is then inverse transformed back to the original data space to obtain a set of raw target signals without contamination from other nearby targets or clutter. The resulting signals can then be reprocessed into a full image of the target area with the isolated target only or into another non-image space. The basic algorithm includes a user-friendly routine to simplify the signal isolation by allowing the user to select the region relevant to a given target using a mouse-drawn box. The effectiveness of the signal isolation was checked by demonstrating that subtracting the isolated target signals from the original data eliminates only the selected target from the original image, as illustrated in Fig. 32. Provided targets are separated by a great enough distance to be resolved by beamforming and care is used in cropping the target in image space, very good isolation is expected. This technique was used extensively to process acoustic color plots from the 2010 pond measurement. Typically, to maximize measurement efficiency, 5-6 targets were deployed simultaneously with only 1-2m separation in the target area, resulting in significant overlap of target signals in the raw data so that standard processing of acoustic color for individual targets would be unavoidably contaminated.

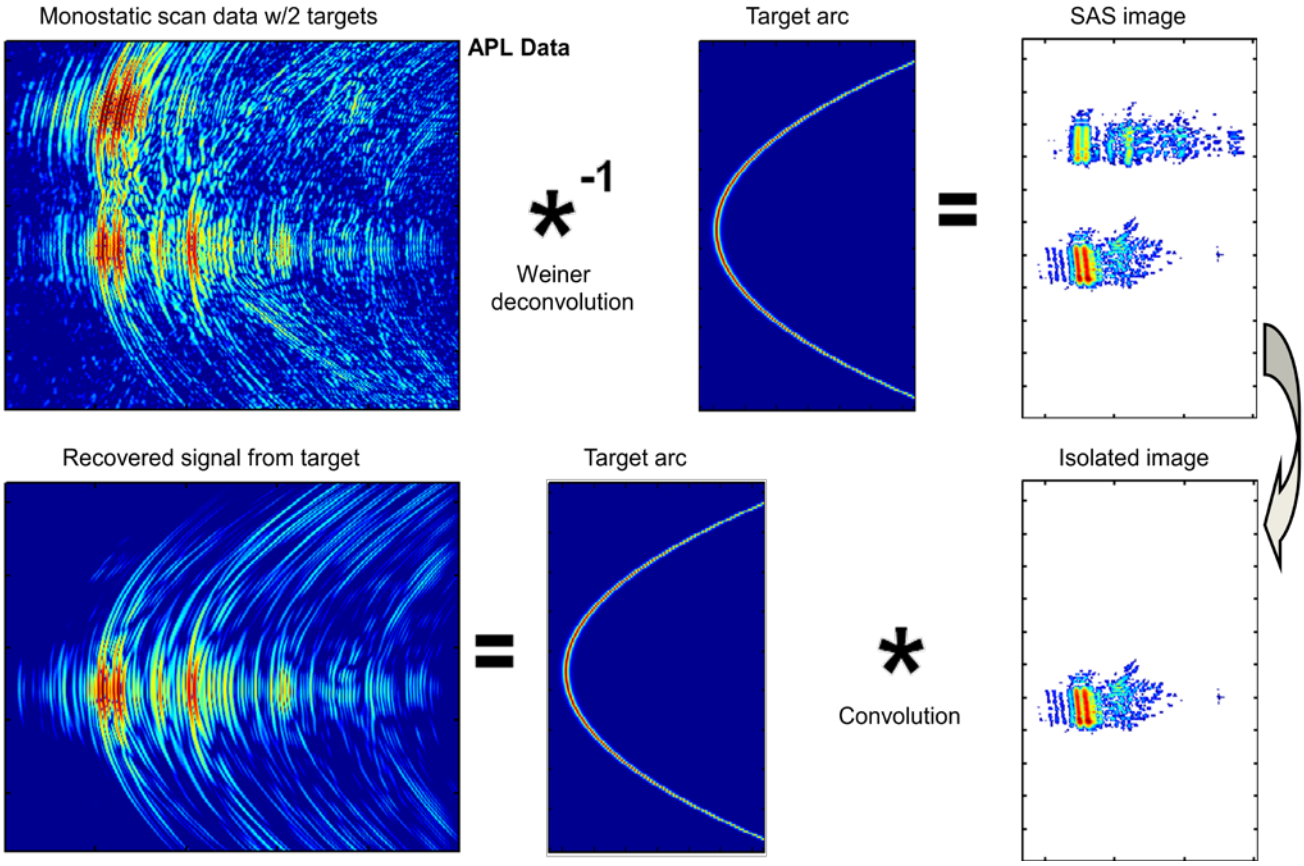


**Figure 31. Isolation of selected target signals from noisy data.**

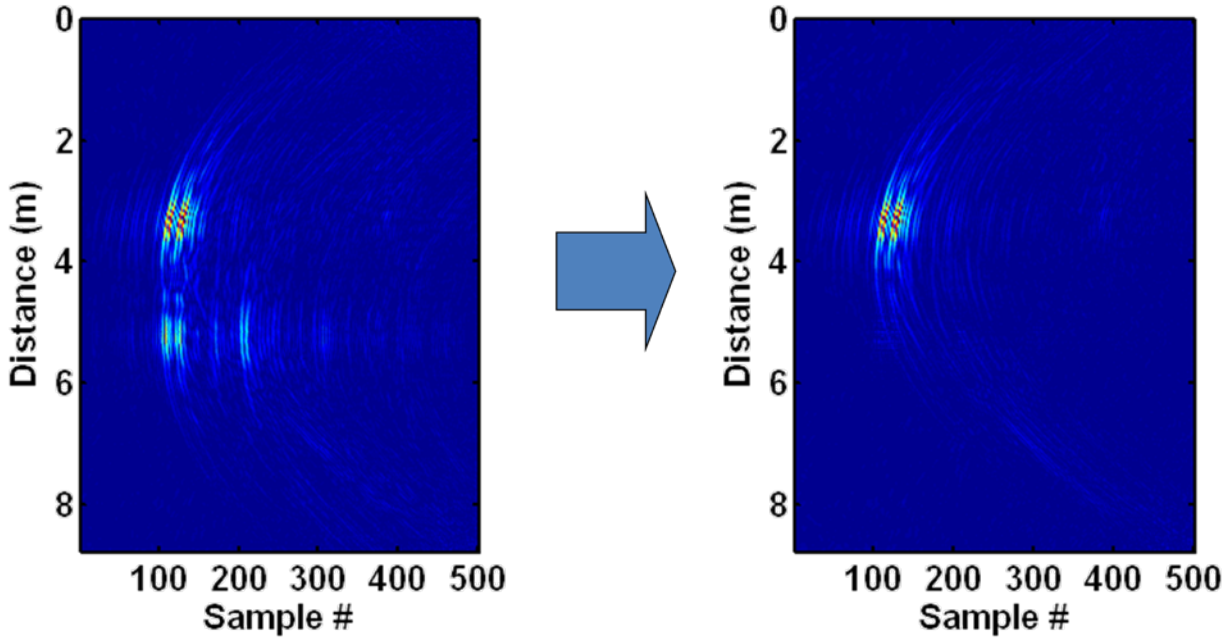


**Figure 32. Subtracting the isolated target signal from the original signal.**

A tool was also developed to help select optimal features for class separation among similarly shaped targets (G. Dobeck, NSWC PCD). The rationale for looking at these types of targets is to help isolate specular phenomena from elastic ones so that the value of classification features derived from the last can be studied. This would be relevant for distinguishing UXO of the same type that are live versus inert. Figure 33 illustrates the variation possible. The top row shows measured free-field target strength plots as a function of frequency and aspect angle for three 2ft-long by 1ft-diameter cylinders of differing material construction. In the bottom row, potential features are shown for each cylinder in the frequency/aspect space. White areas correspond to regions where the corresponding target exhibits target strength at least 3dB higher than the other two. Black areas correspond to regions where the corresponding target exhibits target strength at least 3dB lower than the other two. Gray areas indicate common target strength levels. At least for this limited data set, it is clear that extracting features from the non-gray areas should result in effective separation of any of the 3 targets shown from the remaining two with no error. Of course, a more practical discriminator would be able to distinguish these targets from a feature set measured under a variety of conditions. While 3dB was chosen here as the threshold for highlighting discriminatory phenomena in the target's acoustic color space, it is anticipated that increasing this threshold can help find phenomena to extract more optimal features for use in a classifier being trained with target data collected under a variety of conditions.

In addition to the tools above for augmenting a statistically-based classification process, a physics-based technique was investigated for distinguishing between a similar set of 4 cylindrical targets (R. Arietta, NSWC PCD). Physics motivated classification can help mitigate training requirements if robust signatures can be identified for the desired targets. In this study, the excitation of elastic surface waves was used to distinguish between 4 2ft-long by 1ft-diameter cylinders of differing material construction. Data for this study were from high grazing angle

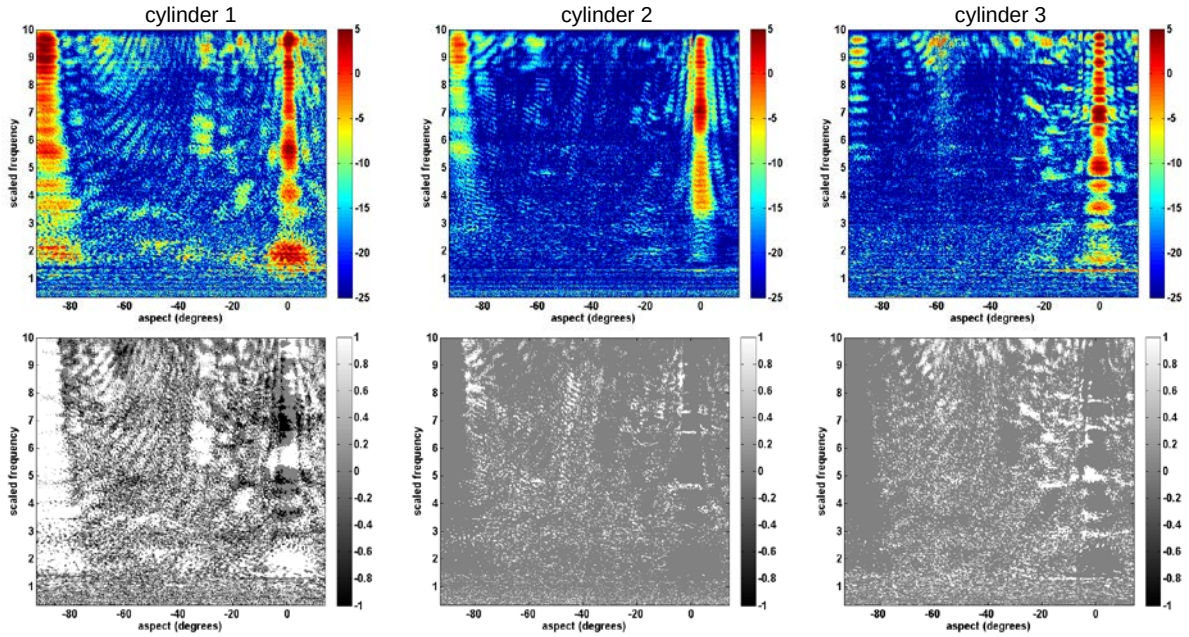


**Figure 33. Among a set of 3 like- shaped cylinders, a feature selection tool is applied to look for phenomena in the acoustic color of each target (top row) that is unique to that target (white or black regions in the corresponding plot below).**

(45$^o$ and 34$^o$) backscatter measurements on these targets deployed proud on the bottom of the NSWC PCD pond in 2009. Target strength plots for the isolated targets exhibited quasi-periodic spectral enhancements over a range of aspect angles that are attributed to dispersive surface borne Rayleigh or Lamb-type elastic waves excited and traveling along a path that navigate around the cylinder until they reach an end, reflect, and then travel towards the other end of the cylinder while radiating back towards the source/receiver. This dynamics is illustrated in Fig. 34 for one of the cylinders studied constructed of solid Al. The spectral properties of the reradiation due to these elastic phenomena are unique to the material makeup of the structure so they should be useful for discrimination.

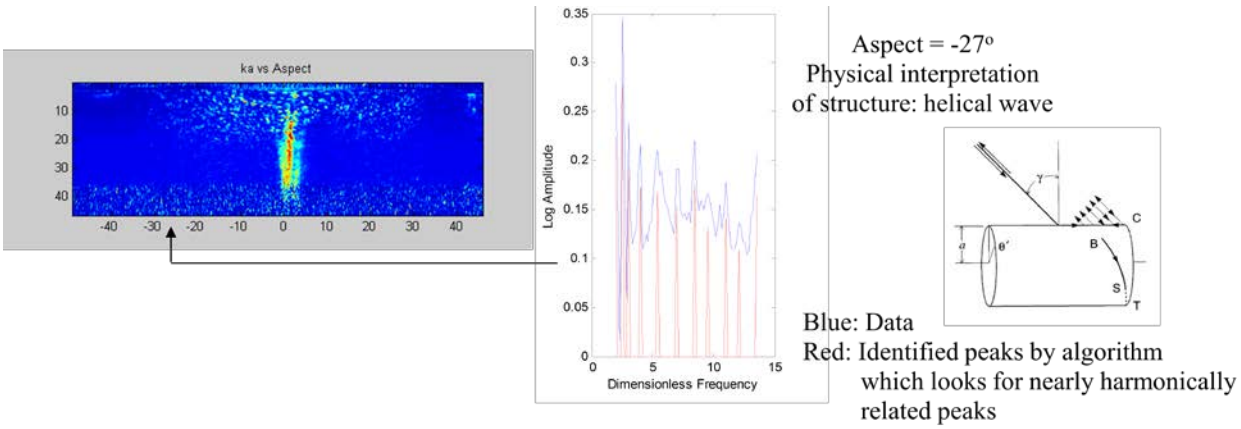


**Figure 34. Excitation of surface Rayleigh waves at -27$^o$ target aspect on a solid Al cylinder produces quasi-periodic structure in its target strength plot.**

To make use of these phenomena, features associated with them need to be extracted. This was done by selecting aspects from the target strength plots that exhibited spectral peaks with a certain spacing consistent with the acoustic coupling angle and surface propagation path and that also exhibited a specified minimum number and magnitude relative to the background. The associated pings for the 4 targets were then inspected by an algorithm that creates feature vectors consisting of a user selected list of values. For the present study, 5 elements were extracted: number of quasi-harmonic peaks, start frequency, separation between peaks, a salient factor (value dependent on relative size of peaks relative to the background), and aspect angle. These 5-element feature vectors from each target were fed into a K-means clustering algorithm, which can group the vectors into N clusters where N is a value that can be set to the number of different targets if this is known or a value iterated in a loop to determine the best clustering if the number of different targets is not known. This process is illustrated in Fig. 35. By setting N=4 for this initial study, the discriminatory power of the selected features was determined to be good since each cluster contained vectors for one target only. Furthermore, as shown in Fig. 36, a MATLAB generated silhouette plot for the clusters demonstrated good confidence in the assignments for the vectors in each cluster. The silhouette value for each feature vector is a measure of how similar that vector is to those in its own cluster compared to vectors in other clusters. Values range from -1 to +1 with high values indicating similarity within a cluster.

Of course, despite the good results, a caveat to this study is that it is based on a limited amount of data collected under conditions that allowed good SNRs on the targets included. Further study with data collected under more difficult conditions and/or more realistic shapes is needed. The effect of different feature vectors that include more peak related information (e.g., trends in peak heights and variability in peak spacing) can also be tried to improve classification performance if needed.

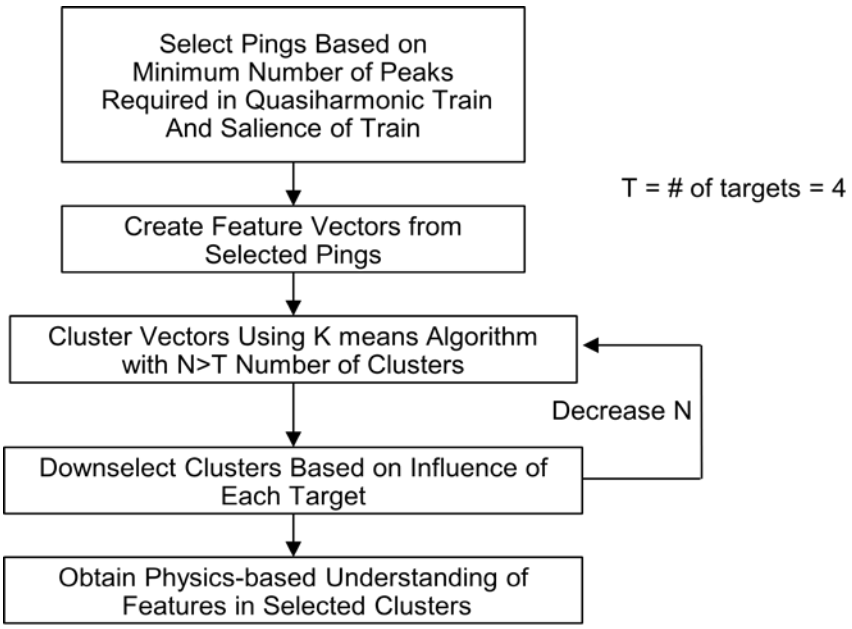


**Figure 35. Process for using elastic information in sonar data to discriminate between 4 cylindrical targets with the same size and shape.**

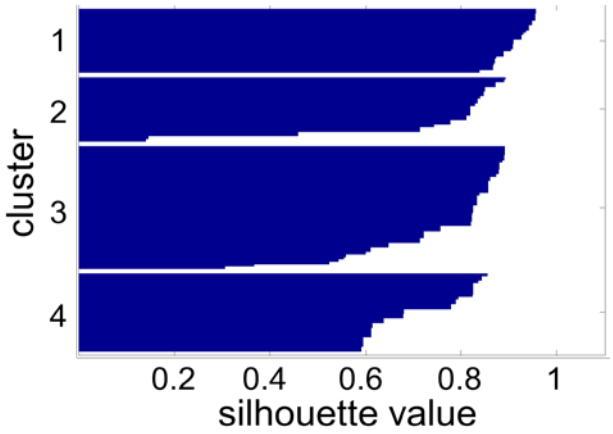


**Figure 36. Silhouette plot of four clusters in 5 dimensional feature space.**

Although the approach taken above seems to work well when the target strength has good SNR across a sufficient range of aspect angles and the surface elastic wave structure is apparent, this may not be the case for small or buried targets or targets for which this structure is corrupted by nearby clutter. Since UXO may be clustered in a relatively small area, corruption is easily possible so another classification approach was sought in 2011 (R. Arietta, NSWC PCD) that only makes use of return signals with no ambiguity of assignment to targets. This is most easily accomplished by looking at the strong returns that go into producing the SAS image. This is the region of interest (ROI) of the target. Here it is assumed that, in most runs past a target, a SAS system will encounter at least one aspect orientation of the target that produces a strong ROI; e.g., near broadside.

A study was carried out to test the feasibility of class separation using time-frequency phenomena extracted from strong ROIs in target scattering data. In general, backscattered signals contain specular as well as structural information that can be difficult to interpret if analyzed strictly in the time or the frequency domains. Time-frequency representations characterize signals simultaneously in both domains and can aid in the physical interpretation of backscattered chirps. However, these two dimensional representations force trade-offs in resolution, computational efficiency, noise reduction, and cross-term generation. Since our goal is the isolation of physically meaningful features that will aid in the classification of targets, we are mainly concerned with the ability of the time-frequency transform to reject noise, but we are also concerned with the effect of the cross-term artifacts that do not represent real phenomena on the ability to classify targets using machine learning approaches.

The time-frequency distributions chosen for our study were based on several criteria that preserve the underlying physical phenomena. Fundamentally the chosen representations had to distribute the energy of the signal along time and frequency. These quadratic transformations of the signals lead to complicated cross-terms when there are multiple sub-signals evolving in frequency. One important criterion is the preservation of time and frequency shifts. Another set of related properties are the conservation of energy and the marginal properties of the distributions that allow the energy spectral density and instantaneous power to be obtained as marginal integrations. The last important criterion is the compatibility with the linear systems approach normally used to deal with the properties of the data collection system and propagation

medium. Another criterion that is not as important as the previous ones in terms of physical meaningfulness but is important in terms of interpretability of the data based on our preferred transmit signal is the perfect localization of a linear chirp.

All of these qualities are available from the Wigner-Ville and related distributions. However, it seems that the presence of these properties in a distribution and the production of cross-terms are intricately linked. Our approach to separate the auto-terms from the cross-terms is based on a comparison of a native time-frequency distribution with its reassigned version. The reassignment method redistributes the values of the integration process such that the energy is assigned to the energy centroid of the local region and not the geometric center of the region as in the native transform. For instance the Wigner-Ville time frequency distribution is compared to its reassigned version in order to isolate the auto-terms from the cross-terms. These two subparts are then independently used in a segmentation process in order to determine the classification value of each. Preliminary results show that the cross-terms do have machine classification value mainly because they tend to spread the signature of a target over a greater area of the time-frequency plane. By using both the native and reassigned distributions it may be possible to obtain the best of both worlds and have a human-interpretable image as well as a machine interpretable one.

Figure 37 presents an example of a simple segmentation scheme used to class separate data from 5 targets. Backscatter UXO data collected in 2010 in the NSWC PCD pond were used in this study (upper left plot of Fig. 37). First, strong backscatter returns available for a particular target were identified. The target in the example is the Al shell replica shown in Fig. 5. Synthetic aperture image processing of the field was used to limit the ROI for this target both in range and aspect (shaded in Fig. 37) since signals from the deployed line of targets overlapped in each data collection run. Within this ROI are a set of pings from which a random subset (50-80) was used to produce a partition of the time-frequency plane that contained disjoint sets of time-frequency regions unique to each target. To do this, a time-frequency distribution plot is created for each ping in the target ping subset, the resulting plots are thresholded at a chosen level, and then overlaid to produce an intermediate template containing common high energy regions for each target. As an example, the sample red ping from in Fig. 37 is windowed and transformed to produce the time-frequency distribution plot in the upper right of Fig. 37. Regions in this plot with intensity beyond a specified level are mapped onto a template like that in Fig. 37, lower left. The set of templates created for each target are combined to form the intermediate template of high energy regions common to all. A template of disjoint high energy regions is then created for each target by removing regions that overlap with regions from templates of dissimilar targets. Each target was represented by a template formed from a subset of these regions.

To test the separability of the targets based on these templates, 5 to 10 random pings were selected that were outside the original subset used to create the templates but were from each target's high backscatter ROI. Segment highlights were extracted from each of these pings. A composite of these highlights such as illustrated in Fig. 37, lower right, was then used to test against the time-frequency templates and scored by how well they were covered by them. An example of this scoring is presented in the bar graph of Fig. 38, where 8 pings from each target

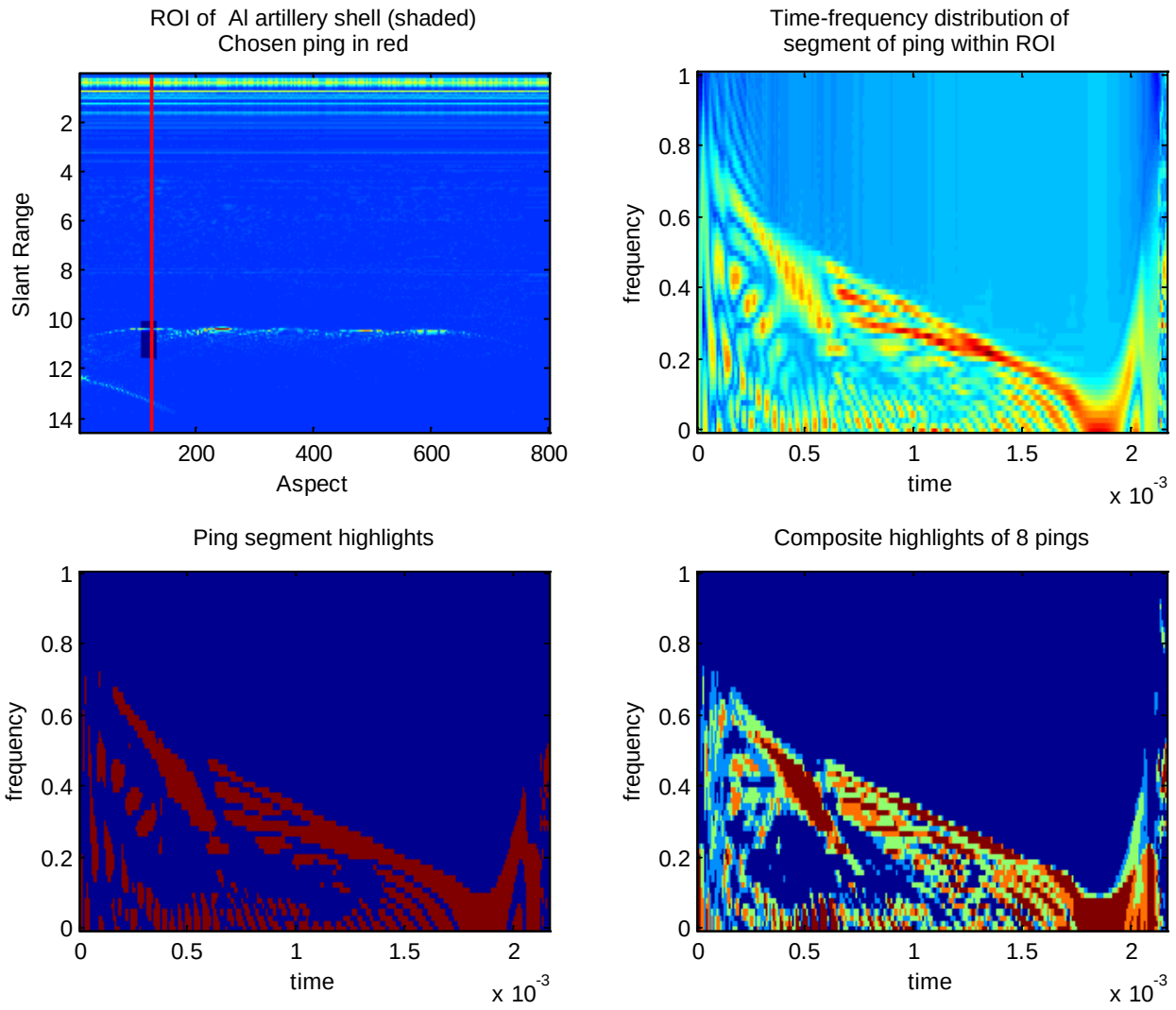


**Figure 37. An example of time-frequency processing of data (upper left) collected in NSWC PCD's pond facility for the Al artillery shell. The time-frequency transform of a windowed segment of the red ping is shown in the upper right. A thresholded template is shown in the lower left. A composite of 8 templates are overlaid in lower right.**

were used to class separate the 5 targets captured in the data. Performance is seen to be good, albeit for a limited data set. This procedure was carried out with several different time-frequency methods in order to determine the importance of the method's resolution, noise reduction quality, and cross-term artifacts, in producing robust time-frequency plane partitions that may be used to classify the targets.

In ongoing study of the use of time-frequency regions for classification, analytical models of simple cylindrical targets have been used to try to assign regions based on an "ideal" partitioning. Modeled target responses yield time-frequency distributions that visually appear quite similar to experimentally derived ones. By comparing the experimentally derived disjoint regions of the time-frequency plane with ones that are derived from modeled cylinders of the same gross dimensions, one can attempt to partition the time-frequency plane of real "cylinder-

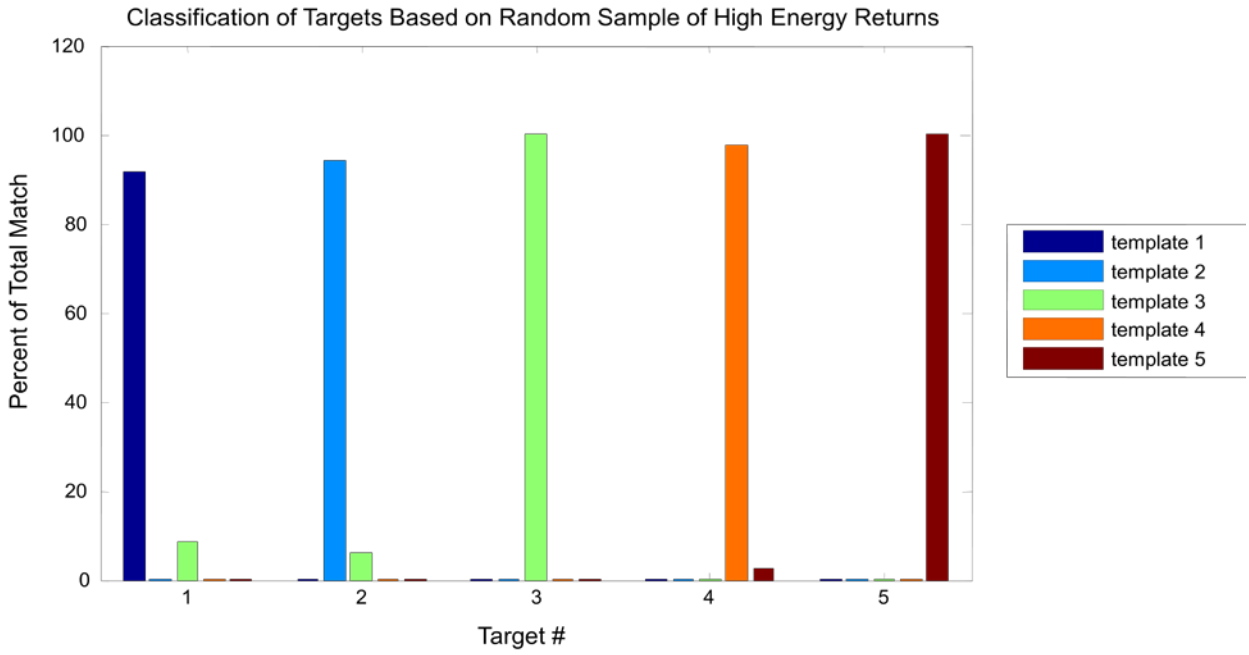


**Figure 38. Bar graph demonstrating class separation of data from 5 targets based on templates of high intensity regions in time-frequency space. Percent match is computed as the ratio of the target template area overlapping segment highlights of the test ping to the total target template area. The % match averaged over all 8 pings in the random set is shown above.**

like" targets into areas that match the idealized results and those that do not. It is hoped that this comparison will allow separation of the time-frequency areas into at least two types of regions. The time-frequency regions sought include those that will allow classification of an object as a man-made (cylinder-like) target and regions that are more closely associated with the specific type of target. While separations like this often look promising on limited data sets, its robustness remains to be verified in future work.

## Rescoped Efforts

A plan to rescope a sonar performance study originally scheduled in 2010 but cancelled due to data distribution issues was approved by SERDP in 2011 to encompass both more data collection from UXO in NSWC PCD's pond facility and the design and acquisition of a new sediment tank as part of an existing pier facility to be used in future high-grazing angle sonar tests against small UXO. Although most of the data collected on UXO during 2009-10 were at shallow grazing angles, high grazing angle data was also collected over a broad aspect range on a set of 5 real UXO shapes at proud and flush buried configurations using the setup in Fig. 4. The additional data collected in 2011 completed a series of half-buried, high-grazing angle target measurements on four UXO targets (see Fig. 5): the Al projectile replica, the steel projectile replica, the 155 mm howitzer shell, and the slotted Al cylinder. Monostatic SAS data was collected using sources and receivers mounted on NSWC PCD's rail. Two targets at a time were deployed and rotated from -80 to +80 degrees in 20 degree steps. The data collected have been processed into 2-dimensional color target strength plots as a function of frequency and aspect angle. These have

been added to the database being circulated to promote model validation, physics analysis, and development of non-image classifiers.

Remaining funds were used to design and purchase a sediment tank for an acoustic pier facility to be refurbished during 2012-13 under other funds. The NSWC PCD test pier extends out into a small brackish pond that is nominally 20 ft deep. The area used for testing is protected from weather and a vinyl liner is used to maintain a freshwater pool that extends the full depth of the pond. Over head rails allow a motorized rotator carrying targets or sonar hardware to be positioned over the test area and lowered into the water. Figure 39 shows a schematic plan of the refurbished facility including placement of the tank to be installed inside the vinyl pool liner. Figure 40 shows a drawing of the sediment tank itself, which consists of another heavy vinyl liner supported on a frame and resting on a neoprene base. The upper frame is kept level by the adjustable supports along the side and a mechanism that divers can use for smoothing the sediment surface was designed to roll along the top of the tank frame. A design study carried out to address resolution of all construction, cost, and installation issues has been completed. The tank is designed to be nominally 21.5 ft square and hold a 3 ft layer of sediment. Funds for purchase and installation of the tank components have been committed through one of NSWC

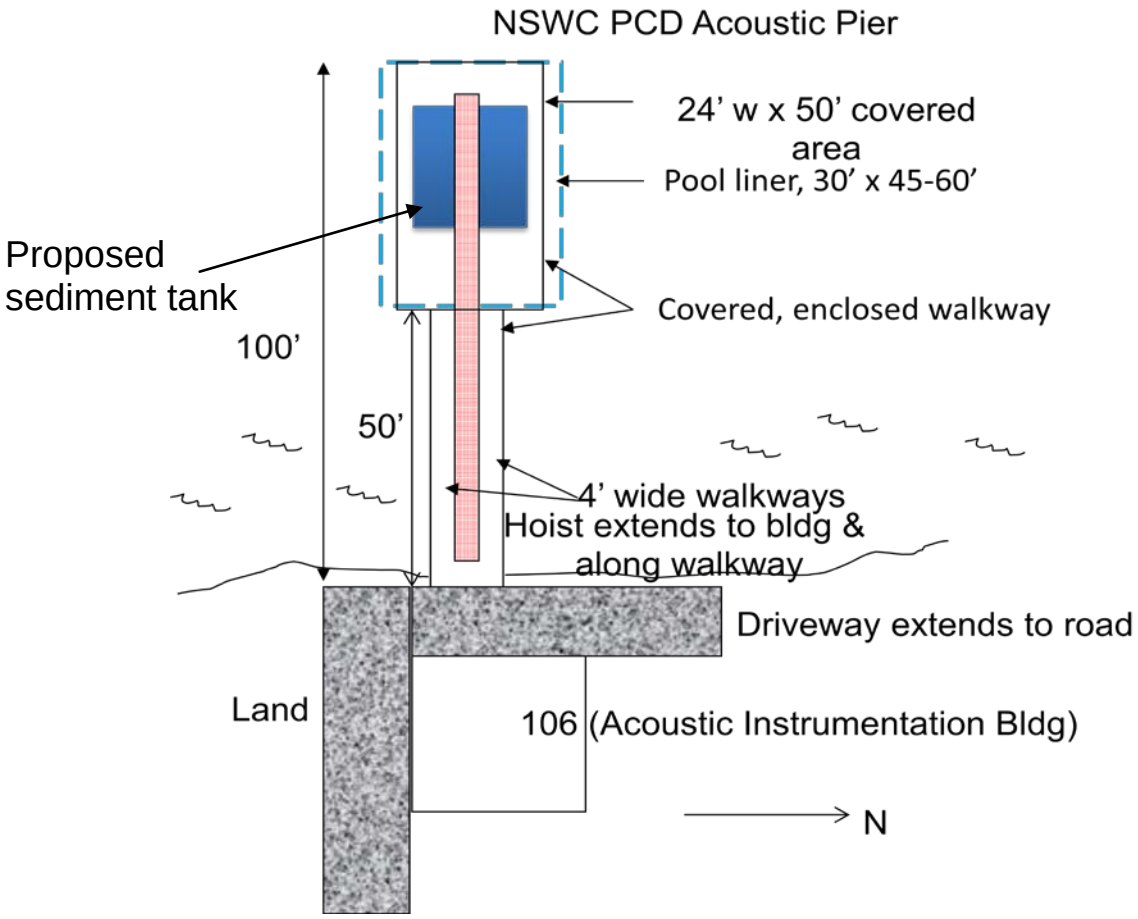


**Figure 39. Schematic of the NSWC PCD Acoustic Pier Facility including the sediment tank (blue) to be deployed at the bottom of the lined freshwater pool. Sonar hardware suspended from the rotator moved along the overhead rail (red) would be able to detect targets in the tank at high grazing angles.**

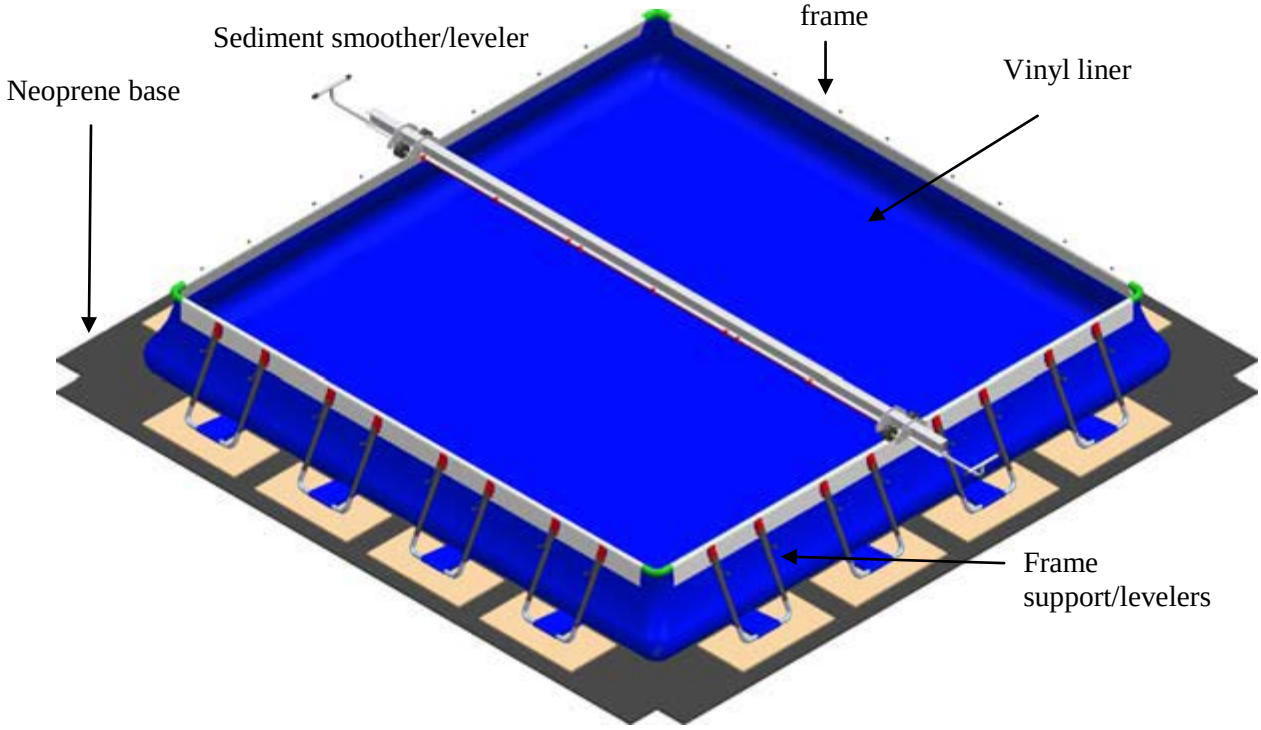


**Figure 40. Pictorial of the sediment tank designed for high-grazing-angle data collection from bottom targets.**

PCDs cost centers and the purchase is scheduled to be executed in 2013 to coincide with completion of the pier refurbishment. This is believed to be a valuable investment for future data collection because the amount of data needed to train automated target recognition algorithms can be large and any means of simplifying the data collection will pay off significantly in the long run.

## Conclusions

Work performed under SERDP project MR-1666 continued to work towards a high fidelity simulation capability that can be used to test overall performance of new sonar designs operated under realistic conditions. However, detection and classification of more problematic UXO (e.g., those that are small and difficult to image) will likely need additional processing tools beyond sonar imaging to be effective. To deal with these UXO, ways to predict the performance of sonar configurations that extract more information from target responses and capture these responses in ways that yield higher SNR were considered. Concepts explored made increasing use of projections of target sonar responses onto non-imaging spaces that don't require high spatial resolution to determine what the target is. Furthermore, the target responses considered were not limited to backscatter since higher SNR is possible in bistatic detection configurations. In fact, tank measurements of free-field forward scattering from cylindrical targets suggest the possibility of isolating strong elastic clues from the source field contamination that usually precludes using this configuration. Predicting performance under these conditions is based on the use of tools such as statistical classification algorithms that require a large amount of data to train and test with. Otherwise, misleading, often overly optimistic, results can be produced.

The efforts carried out have focused on ways to enhance existing target response databases for physical analysis and testing and training of classification tools. This included continued collection and processing of target data on several UXO and clutter in NSWC PCD's pond facility and creating a capability to calculate target responses with FE. A long-term goal will be to supplement UXO sonar response measurements with accurate FE simulations so this capability has been developed in a systematic manner, with comprehensive verification and validation studies to ensure sufficient efficiency, speed, accuracy, and ease-of-use can be achieved. The FE capability at NSWC PCD has reached sufficient maturity to carry out simulations for targets of realistic complexity. Production level simulations of target strength plots for several clutter and UXO targets have been produced, including a flat-end-capped solid Al cylinder, an empty, flat-end-capped cylindrical shell, WSU's "paddle" target, and the 100 mm projectile in Fig. 2 in a sand bottom.

Software tools were also developed to imbed target responses into realistic environments using PC SWAT and to increase the efficiency of data collection, processing of target representation schemes, and target classification. These tools have been used to supplement the data available but, because some simplifying approximations were made in implementing these tools, they will continue to be studied as needed to fully assess their impact. Nevertheless, their value for increasing classifier effectiveness is expected to be significant when compared to the expense of field surveys for providing the data otherwise required.

In recent work, the efforts performed continue to expand and improve our understanding of the physics useful for classification. Initial studies using sonar-derived features based on physics unique to a target's composition has shown good performance in being able to remotely separate four cylindrical targets of the same size but different material construction when deployed on a sand bottom. This might be relevant to discriminating live from practice UXO rounds. While the features chosen were only used with a limited dataset, the potential for mitigating some of the training requirements of purely statistical approaches is clear. Physics can be used to identify phenomena to derive features from that are less sensitive to environmental effects. If environmental effects cannot be avoided, it may still be more efficient to tune a classifier using physics to predict the effect on the features used than to collect more data for further training.

In addition, further classification analysis based on non-imaging target representations have been looked at. Time-frequency distribution plots were shown to be useful for distinguishing the targets deployed in NSWC PCD's pond in 2010. When target signals are not strong over sufficiently wide target aspect windows, these plots may provide more useful information for classification by exploring the time dimensions at strong aspects for target features. Both NSWC PCD and APL-UW (K. Williams) have written MATLAB routines for accessing much of the 2010-11 pond data, including the software for isolating targets (T. Marston) and generating target strength plots, so that features can be derived from them and input into classifiers. These have been also distributed to other NSWC PCD classification specialists not supported by SERDP to encourage use of the UXO data in testing their ATR algorithms.

# References


1. A. Wood and E. Weston, "The propagation of sound in mud," *Acustica* **14**, pp. 156-506, 1964.

2. A. D. Pierce and W. M. Carey, "Card-house theory of mud sediments containing kaolinite and its acoustical implications," *POMA* 5 070001 (2009).

3. W. M. Carey, "Sound Propagation in Muddy Sediments," BU Final Technical Report and Final Report of Inventions and Subcontracts for grant N61331-07-1-G001. (attached in Appendix)

4. K. L. Williams, S. G. Kargl, E. I. Thorsos, D. S. Burnett, J. L. Lopes, M. Zampolli, P. L. Marston, "Acoustic scattering from a solid aluminum cylinder in contact with a sand sediment: measurements, modeling, and interpretation," *J. Acoust. Soc. Am.* **127**(6), 3356-71, 2010.

5. S. G. Kargl, K. L. Williams, T. M. Marston, J. L. Kennedy, and J. L. Lopes, "Acoustic Response of Unexploded Ordnance (UXO) and Cylindrical Targets," Proceedings of MTS/IEEE Oceans 2010, Seattle, WA, Sept. 20-23, 2010.

6. M. Soumekh, **Synthetic Aperture Radar Signal Processing: with MATLAB Algorithms**, John Wiley & Sons, 1999.

# APPENDIX

List of SERDP Technical Publications

Technical Reports:


1. A. D. Pierce and W. M. Carey, "Card-house theory of mud sediments containing kaolinite and its acoustical implications," *POMA* 5 070001 (2009).
2. J. E. Piper, R. Lim, E. I. Thorsos, and K. L. Williams, "Buried Sphere Detection Using a Synthetic Aperture Sonar," *IEEE Journal of Ocean Engineering* **34**(4), 485-494, 2009.
3. K. L. Williams, S. G. Kargl, E. I. Thorsos, D. S. Burnett, J. L. Lopes, M. Zampolli, P. L. Marston, "Acoustic scattering from a solid aluminum cylinder in contact with a sand sediment: measurements, modeling, and interpretation," *J. Acoust. Soc. Am.* **127**(6), 3356-71, 2010.
4. D. S. Burnett, "Absorbing boundary conditions for the acoustic Helmholtz equation for ellipsoidal, spheroidal and spherical domain boundaries," submitted to *J. Acoust. Soc. Am.*
5. W. M. Carey, "Sound Propagation in Muddy Sediments," BU Final Technical Report and Final Report of Inventions and Subcontracts for grant N61331-07-1-G001, 2011.


Conference/Symposium Proceedings


1. S. G. Kargl, K. L. Williams, T. M. Marston, J. L. Kennedy, and J. L. Lopes, "Acoustic Response of Unexploded Ordnance (UXO) and Cylindrical Targets," Proceedings of MTS/IEEE Oceans 2010, Seattle, WA, Sept. 20-23, 2010.


Published Technical Abstracts:


1. R. Lim, J. Lopes, I. Paustian, R. Arietta, G. Dobeck, and D. Burnett "Pond Measurements to Investigate Sonar Detection and Classification of Underwater UXO," Partners in Environmental Technology Technical Symposium and Workshop, Washington, D. C., 1-3 Dec, 2009.
2. R. Lim, J. Kennedy, T. Marston, R. Arrieta, I. Paustian, and J. Lopes, "Sonar Measurements and Processing to Facilitate Detection and Classification of Underwater UXO," Partners in Environmental Technology Technical Symposium and Workshop, Washington, D. C., 30 Nov-2 Dec, 2010.
3. H. Johnson, D. S. Burnett, K. Lee, and D. Sternlicht, "High-fidelity Active-acoustics Modeling for Anti-mine and Anti-submarine Warfare," National Defense Industrial Association Joint Undersea Warfare Technology Conference, San Diego, Mar 2012.
4. R. Lim, G. S. Sammelmann, and J. L. Lopes, "Wavefront curvature and near-field corrections for scattering by targets buried under sea-floor ripple," *J. Acoust. Soc. Am.* **125**(4), Pt. 2, 2733 (2009).
5. J. Lopes, K. Williams, S. Kargl, T. Hefner, E. Thorsos, P. Marston, I. Paustian, and R. Lim, "Monostatic and bistatic measurements of targets resting on or buried under the seafloor," invited presentation, *J. Acoust. Soc. Am.* **125** (4), Pt. 2, 2701 (2009).
6. D. S. Burnett, "Acoustic color of elastic objects near boundaries: High fidelity, high speed, 3-D finite-element modeling," invited presentation, *J. Acoust. Soc. Am.* **125** (4), Pt. 2, 2701 (2009).
7. S. G. Kargl, K. L. Williams, A. L. Espana, J. L. Kennedy, T. M. Marston, J. L. Lopes, and R. Lim, "Acoustic scattering from underwater munitions near a water-sediment interface," invited presentation, *J. Acoust. Soc. Am.* **129** (4), Pt. 2, 2685 (2011).

8. R. Holtzapple, “Bluefin12 buried mine hunting system,” invited presentation, *J. Acoust. Soc. Am.* **129** (4), Pt. 2, 2663 (2011).
9. W. Carey and A. D. Pierce, “Sonic speed estimates for muddy sediments with plausible microbubble distributions,” *J. Acoust. Soc. Am.* **129** (4), Pt. 2, 2389 (2011).
10. R. Arrieta, R. Holtzapple, and R. Lim, “Comparison of time-frequency distributions for target classification,” *J. Acoust. Soc. Am.* **129** (4), Pt. 2, 2664 (2011).
11. J. R. La Follett, P. C. Malvoso, and R. Lim, “Bistatic scattering by scaled solid metallic objects: Circular line-scan measurements and modeling,” *J. Acoust. Soc. Am.* **130** (4), Pt. 2, 2554 (2011).
12. W. M. Carey and A. D. Pierce, “Sound speed, pulse spreading, and reverberation in muddy bubbly sediments,” *J. Acoust. Soc. Am.* **130** (4), Pt. 2, 2555 (2011).
13. A. D. Pierce and W. M. Carey, “Acoustic scattering by bubbles in naturally occurring mud sediments,” *J. Acoust. Soc. Am.* **130** (4), Pt. 2, 2555 (2011).
14. A. L. Espana, K. L. Williams, S. G. Kargl, M. Zampolli, D. S. Burnett, and P. L. Marston, “Acoustic scattering from unexploded ordnance in contact with a sand sediment: Mode identification using finite element models,” *J. Acoust. Soc. Am.* **130** (4), Pt. 2, 2330 (2011).

## Why is sound slower in mud?

$$V = V_s + V_f \quad \rightarrow \rho = \rho_s V_s / V - \rho_f V_f / V \qquad \rho = \rho_s f_s + \rho_f f_f$$

$$-(1/V)\partial V/\partial P = -(V_s/V)(1/V_s)\partial V_s/\partial P - (V_f/V)(1/V_f)\partial Vf/\partial P$$

$$\rightarrow K = f_s K_s + f_f K_f \qquad \rightarrow 1/B = f_s/B_s + f_f/B_f$$

$$With\ C^2 = B/\rho$$

$$1/C^2 = (\rho_s f_s + \rho_f f_f)(f_s/B_s + f_f/B_f)$$

$$C_f^2/C^2 = (1 + (\rho_s/\rho_f - 1)f_s)(1 - f_s(1 - B_f/B_s))$$

The Mallock – Wood Equation,[1,2]

Measurements of the sound speed characteristic of the high porosity Dodge Pond mud were found to have a sonic speed less than that observed by Wood and Weston [3], a compressional speed 3% less than that of water. Other experiments performed on muddy sediments at frequencies greater than a kilohertz are consistent with the Dodge Pond observations when microbubbles are present. The presence of bubbles is known to be an important factor in decreasing the sound speed. A theoretical treatment of "muddy sediments", the Card House Theory (Pierce and Carey, [4]), estimated the slow sound speed and frequency dispersion proportional to mud porosity, $C_{mud}$ approximately (0.91-0.97)$C_w$. The presence of a micro-bubbles can lower the sound speed consistent with the Mallock -Wood equation when the bubble size distribution and mean bubble separation are less than the wavelength of the propagating wave.

[1] Mallock,A.,(1910) "The damping of sound by frothy liquids," Proc. R. Soc. London, Ser. A 84, 391–395 (1910).

[2] Wood, A. B. ,(1941) A Textbook of Sound, 2nd ed. (Macmillan, New York, 1941), pp. 360 –362.

[3] Wood, A. and E.Weston, (1964)"The propagation of sound in mud", Acustica 14,156-506, 1964.

[4] Pierce, Allan D. and William M. Carey, (2009) "Card-house theory of mud sediments containing kaolinite and its acoustical implications ", POMA 5 070001 (2009)

# Acoustic scattering from a solid aluminum cylinder in contact with a sand sediment: Measurements, modeling, and interpretation

Kevin L. Williams, Steven G. Kargl, and Eric I. Thorsos
*Applied Physics Laboratory, College of Ocean and Fishery Sciences, University of Washington, Seattle, Washington 98105*

David S. Burnett and Joseph L. Lopes
*Naval Surface Warfare Center, Panama City Division, Panama City, Florida 32407*

Mario Zampolli[a)]
*TNO Defense, Security and Safety, Oude Waalsdorperweg 63, P.O. Box 96864, 2509 JG The Hague, The Netherlands*

Philip L. Marston
*Department of Physics and Astronomy, Washington State University, Pullman, Washington 99164*

(Received 14 December 2009; revised 5 April 2010; accepted 8 April 2010)

Understanding acoustic scattering from objects placed on the interface between two media requires incorporation of scattering off the interface. Here, this class of problems is studied in the particular context of a 61 cm long, 30.5 cm diameter solid aluminum cylinder placed on a flattened sand interface. Experimental results are presented for the monostatic scattering from this cylinder for azimuthal scattering angles from 0° to 90° and frequencies from 1 to 30 kHz. In addition, synthetic aperture sonar (SAS) processing is carried out. Next, details seen within these experimental results are explained using insight derived from physical acoustics. Subsequently, target strength results are compared to finite-element (FE) calculations. The simplest calculation assumes that the source and receiver are at infinity and uses the FE result for the cylinder in free space along with image cylinders for approximating the target/interface interaction. Then the effect of finite geometries and inclusion of a more complete Green's function for the target/interface interaction is examined. These first two calculations use the axial symmetry of the cylinder in carrying out the analysis. Finally, the results from a three dimensional FE analysis are presented and compared to both the experiment and the axially symmetric calculations. 
[DOI: 10.1121/1.3419926]

PACS number(s): 43.30.Jx, 43.40.Fz [NPC] Pages: 3356–3371

## I. INTRODUCTION

Scattering from elastic objects placed on or near the water/sediment interface is a problem receiving increasing attention.[1–5] In many cases the targets of interest have been hollow spheres. This focus on spheres has been, in part, because numerical and analytical modeling of the target is well-developed; thus one can concentrate on the physics introduced by being near the sediment/water interface. However, recent developments in finite element (FE) modeling[4,6,7] now allow examination of more complicated elastic objects placed on the interface between two media.

In this article the target examined is a solid aluminum cylinder with flat ends. The cylinder is 61 cm long and 30.5 cm in diameter. It was placed on a flat sand/water interface (often called the "proud" target case, a terminology that will be used here) and data acquired at frequencies from 1 to 30 kHz over azimuthal angles from 0° (broadside) to 90°. Like the sphere, examination of scattering from finite elastic cylinders in the free field also has a long history from which the physical processes involved in the scattering can be quantitatively understood.[8–11] This insight is valuable for the present case when examining experimental results and when comparing FE modeling to these experimental results.

There are three goals in the present article. The first is to present experimental results for the absolute target strength of the proud cylinder as well as synthetic aperture sonar (SAS) images of the cylinder. These results are important for testing models not only within the rest of this article but hopefully also for models developed by other researchers. The second goal is to explain the experimental results within the context of previous physical acoustics analyses.[10,11] The final goal is to use data/FE model comparisons and the physical acoustics insights to better understand the essential physical processes and geometrical parameters that must be included in FE modeling in order to predict the absolute target strength of a proud cylinder for the geometries realized here.

The remainder of this article is organized as follows. Section II presents a summary of the experimental apparatus and procedure as well as the analyzed results. Section III

[a)]Part of the work presented was carried out while the author was at the NATO Undersea Research Centre, La Spezia, Italy.

# Acoustic Response of Unexploded Ordnance (UXO) and Cylindrical Targets

Steven G. Kargl and Kevin L. Williams
Applied Physics Laboratory
University of Washington
1013 NE 40th St
Seattle WA 98105
Email: kargl@apl.washington.edu

Timothy M. Marston
Physics and Astronomy Dept.
Washington State University
Pullman, WA 99164-2814

Jermaine L. Kennedy
and Joseph L. Lopes
Naval Surface Warfare Center
Panama City Division
Panama City, FL 32407-7001

***Abstract*— A series of monostatic and bistatic acoustic scattering measurements were conducted to investigate discrimination and classification capabilities based on the acoustic response of targets for underwater unexploded ordnance (UXO) applications. The measurements were performed during March 2010 and are referred to as the Pond Experiment 2010 (PondEx10), where the fresh water pond contained a sand sediment. The measurements utilized a rail system with a mobile tower and a stationary sonar tower. Each tower is instrumented with receivers while the sources are located on the mobile tower. For PondEx10, eleven targets were deployed at two distinct ground ranges from the mobile tower system. Acoustic data were initially processed using synthetic aperture sonar (SAS) techniques, and the data were further processed to generate acoustic templates for the target strength as a function of frequency and aspect angle. Preliminary results of the processing of data collected from proud targets are presented. Also presented are the results associated with a processing technique that permits isolation of the response of an individual target, which is in close proximity to other targets.**

## I. Introduction

Although the practice of disposing conventional and chemical munitions in coastal waters was discontinued during the 1970's, the environmental, economical, and even the recreational impact persists today [1]. In Overfield and Symons' overview of the Resources and UnderSea Threats (RUST) database [2], they note that 2100 underwater sites are likely to contain munitions. Of those 2100 sites, verification has been completed on only slightly more than 50%. Schwartz and Brandenburg [3] summarize the current technologies available for underwater UXO applications. Their Table 1 includes metal detection (e.g., electromagnetic induction and magnetometers), chemical sensors (spectroscopy and fluorescence), and sonar. Metal detection and chemical sensors are typically restricted to short ranges; while the sonar technologies considered are limited in range (e.g., Didson system) or are limited by poor penetration into sediments (e.g., side-scan sonar) due to the high frequencies used. Furthermore, Schwartz and Brandenburg note that SAS is still a relatively new technology in UXO detection and that low-frequency SAS systems have demonstrated detection of proud and partially buried objects [4].

Low-frequency SAS systems with a wide bandwidth have several advantages over higher frequency sonar systems. Low frequencies offer greater detection ranges, which permits the surveying of wider areas. In addition, low frequencies attain greater penetration depths into sediments, which permit detection of partially and completely buried munitions. The range resolution of a SAS system is related to the bandwidth of the transmitted signal where a wider bandwidth provides higher resolution. Thus, we report here on our preliminary analysis of UXO detection and discrimination by a low-frequency wide bandwidth SAS system. Our work compliments that of Bucaro *et al.* [4] in that they consider isolated UXO in their research. The experiments conducted during PondEx10 have multiple UXO in the field of view of the SAS system with a minimum separation distance of 1.5 m.

## II. Pond Experiment 2010

PondEx10 was carried out in a fresh water pond located at the Naval Surface Warfare Center, Panama City Division (NSWC PCD). This pond holds approximately 9 million gallons of water, and has nominal dimensions of 110 m in length and 80 m in width. The water depth at the location of the deployed target fields is $\sim 14$ m. A $\sim 1.5$ m thick layer of medium-fine sand covers the bottom of pond. To prevent biological growth and fouling of the targets and equipment, the water is filtered and chlorinated. During the PondEx10 exertions, the sound speed in the water, which was determined from temperature measurements acquired from the divers, was found to be 1456 m/s. A detailed drawing and aerial view of the pond can be found in [5].

Eleven targets were deployed in the measurements. The targets included a solid aluminum cylinder, an aluminum pipe, an inert 81 mm mortar (filled with cement), a solid steel artillery shell, two machined aluminum UXO, a machined steel UXO, a de-militarized 152 mm TP-T round, a de-militarized 155 mm empty projectile (without fuse or lifting eye), a small aluminum cylinder with a notch, and two rocks with sizes comparable to the UXO targets. Figure 1 shows a few of the UXO and generic shapes used. The machined UXO, based on a CAD drawing of the solid steel artillery shell, were constructed from materials with known properties. The aluminum cylinder is 2 ft long with a 1 ft diameter; while the pipe is 2 ft long with an inner diameter of 1 ft and 3/8 inch wall thickness.